

博士論文

DOCTORAL DISSERTATION

**Numerical Simulations for Tensile Properties of Fiber-reinforced  
Polymer Rod Bonded in Anchorage**

(定着された FRP ロッドの引張特性に関する数値シミュレーション)



YAMAGUCHI UNIVERSITY  
山口大学

2022 年 3 月

March 2022

VO VAN NAM

山口大学大学院創成科学研究科

**Graduate School of Sciences and Technology for Innovation,  
Yamaguchi University**



## **Keywords**

Fiber-reinforced polymer rod; Shear-lag effect, Load capacity, Tensile failure mode; Cohesive zone model; Representative volume element.

## Abstract

Fiber-reinforced polymer (FRP) rods fabricated from unidirectional fibers and a polymer matrix strengthen effectively reinforced concrete (RC) members. The pultrusion is a production method of FRP rod. The FRP rods show various advantages, such as light and no-corrosion. Most FRP rods have higher tensile strength than standard steel bars. Therefore, the FRP rods can be used as an alternative reinforcement of steel bars in RC structures. In addition, FRP rods can be applied in near-surface mounted (NSM) systems for strengthening existing concrete structures. The tensile properties of FRP rods in adhesively bonded anchorages are expected to be studied in detail. Numerous experimental studies were conducted on FRP rods made of glass, carbon, aramid, or basalt fibers. The previous studies have reported that the tensile properties of FRP rods are affected by the shear-lag effect. However, these studies referred to the tensile failure, the shear-lag effect of FRP rods as a phenomenon without a mechanical explanation. Moreover, the effects of mechanical properties of fibers, matrix, fiber-matrix interface on FRP rod properties have not been investigated in detail.

To quantify factors affecting the tensile properties of FRP rods, this study performed a numerical investigation on aramid FRP rods to assess the shear-lag effect, tensile load-capacity, and tensile strength. In addition, the effects of fiber, matrix, and fiber-matrix interface on the behavior of FRP material in three dimensions were demonstrated by micro-models. Firstly, two representative volume element (RVE) models of fibers and matrix were proposed to predict engineering constants and strengths of the FRP material in three dimensions. Based on the predicted strength, the criteria were designed. Then, the main simulation, including the FRP rod, the filling material, and the steel tube, was carried out to analyze FRP rods under the variation of interfacial conditions between materials, including full-bonding strength and partially bonding strength models. In the partially-bonding strength model, the interfaces between materials were simulated as cohesive zone models with the variation of bond strengths and fracture energy release rate.

A technique called submodeling was applied to enhance the simulation results. The submodel was cut from the main simulation model and only applied to simulate FRP rods with finer meshes. The study proposed a procedure for calculating the stress distribution in any cross-section of an FRP rod. The simulation results agreed well with the previous experimental study. The findings clearly indicated the position of the failure section in which the tensile stress distribution is unequal.

The load-capacity, failure modes, shear-lag effect were predicted based on the maximum stress criterion. The results revealed that the FRP material strengths enforce the failure in two modes associated with the transverse and longitudinal directions of FRP rods. In addition, diameter is a significant factor that increases the shear-lag effect and reduces the tensile strength of the FRP rods. The numerical simulation provided a new method to predict the load-capacity of FRP rods. The study consists of 6 chapters. Outline of the chapter was presented as follows:

Chapter 1 introduces about kinds of FRP rods and their application in civil engineering. The chapter shows the research objects, the gaps in composite studies, and the scopes of the present research.

Chapter 2 summarizes the review of previous studies related to the theoretical studies of the composite materials. The chapter reveals the gap of theory. In addition, the study compares the advantages and disadvantages of previous studies and proposes methods and models for the present study.

Chapter 3 presents the simulations of the representative volume element (RVE) models to determine the mechanical properties and strengths of composite materials. The study investigates the effects of the fiber properties and fiber-matrix interface on composite mechanical properties in detail. The RVE-1 model was employed to predict engineering constants of the FRP material. The RVE-2 was applied to predict the tensile and shear strengths in three dimensions.

Chapter 4 shows the numerical simulations of the FRP rod tensile tests with various cases of the materials in Chapter 3. The models are built in two cases of the interface between the FRP rod and filling material: full-bonding and partially-bonding strengths. In the case of the full-bonding strength, three models are built with three hypotheses of FRP rod material. Three models, A, B, and C, were proposed to demonstrate the effect of fiber properties on FRP properties. Model A was built based on the hypothesis that the FRP rod is made of transversely isotropic fibers. Model B was made to simulate with an FRP rod of isotropic fibers. Model C assumes the FRP rod as an isotropic material. In the case of the partially-bonding strength, the study models various interface cases between the FRP rod and the filling materials to investigate the bonding effects. The proposed models were applied to simulate FRP rods from D3 to D8 to analyze the diameter effect.

In Chapter 5, the difference between the proposed models was discussed to show the advantages and disadvantages of each model. Firstly, the study compared models (A, B, and C) to highlight the effect of fiber properties on FRP rods. Secondly, the study compared the partially-bonding strength and full-bonding strength models to investigate the bonding effects on the tensile

properties of FRP rods. Moreover, the chapter illustrates the existence of the shear-lag effect and demonstrates the diameter effect on tensile strength in FRP rods.

Chapter 6 summarizes the novel findings and research significance of the study. In addition, recommendations for future works were also presented.

## Table of Contents

Keywords .....	i
Abstract .....	ii
Table of Contents .....	v
List of Figures .....	vii
List of tables .....	ix
List of Abbreviations .....	x
Statement of Original Authorship .....	xi
Acknowledgments .....	xii
Chapter 1. Introduction.....	1
1.1. Background.....	1
1.2. Research objectives .....	3
1.3. Scopes of the research .....	4
1.4. Outline .....	5
Chapter 2. Literature review.....	6
2.1. Determining properties of FRP rods.....	7
2.1.1. Methods based on the rule of mixture formulas .....	9
2.1.2. Methods based on the numerical models .....	12
2.2. Failure criterion and strengths of FRP materials.....	16
2.2.1. Prediction strengths by formulas.....	17
2.2.2. Prediction strengths by RVE models .....	19
2.3. Cohesive zone model.....	22
2.4. Model of FRP rods in bond-type anchorage system.....	24
2.5. Submodeling technique .....	26
2.6. Shear-lag effect in FRP rods.....	27
Chapter 3. RVE modeling .....	29

3.1. Fibers and matrix properties .....	29
3.2. RVE-1 .....	30
3.3. RVE-2 .....	31
Chapter 4. Numerical modeling of tensile tests .....	36
4.1. Materials.....	36
4.2. Numerical models with perfect bond.....	37
4.2.1. Model A results .....	45
4.2.2. Model B results.....	51
4.2.3. Model C results.....	52
4.3. Numerical models with partially-bonding strength .....	53
4.3.1. Failure modes of FRP rods .....	55
4.3.2. Shear-lag effect.....	66
Chapter 5. Discussion .....	71
5.1. Comparison of models A, B, and C .....	71
5.2. Shear-lag effect .....	72
5.3. Diameter effects .....	73
Chapter 6. Conclusions and recommendations .....	75
6.1. Conclusions.....	75
6.2. Recommendations for future works.....	76
References .....	77
List of Publications .....	86

## List of Figures

Figure 1.1. Markets and applications of FRP materials [1].....	1
Figure 1.2. Pultrusion method [3]. .....	2
Figure 1.3. Pultrusion FRP bars [19]. .....	3
Figure 2.1. Micromechanics process [46]. .....	6
Figure 2.2. Stress-strain relationships of fibrous reinforcement and matrix [47].....	7
Figure 2.3. Typical representative volume elements (RVE) for (a) rectangular packing array and (b) hexagonal packing array [46].....	9
Figure 2.4. RVE subjected to longitudinal uniform strain [46].....	9
Figure 2.5. RVE subjected to transverse uniform stress [46].....	10
Figure 2.6. Models to determine the shear moduli [46]. .....	11
Figure 2.7. RVE models of square and hexagonal array distributions [50]. .....	13
Figure 2.8. Hexagonal array RVE model. ....	14
Figure 2.9. RVE models: (a) 2D model [65], (b) 3D model [66].....	20
Figure 2.10. Debonding at fiber-matrix interface and failure under transversal load [69].....	21
Figure 2.11. Random distribution RVE model (RVE-2).....	22
Figure 2.12. Bilinear traction-separation law .....	23
Figure 2.13. Testing system in ASTM D7205/D7205M-06 (2016): (a) example anchor details, (b) dimensions of test specimens and steel tubes, (c) example of the attachment of anchor to grips or threaded collets [72].....	25
Figure 2.14. Tensile model of CFRP rod in bond anchorage system [44]. .....	26
Figure 2.15. Submodeling technique: (a) full model, (b) submodel [54].....	27
Figure 2.16. Shear-lag effect [42].....	28
Figure 3.1. Stress-strain curves of resins.....	30
Figure 3.2. CZM models at fiber-matrix interfaces.....	33
Figure 3.3. Tensile stress-strain curve of the RVE-2 models.....	35
Figure 4.1. Analysis model in ANSYS: (a) half model; (b) divided model (global model). ...	39
Figure 4.2. Boundary conditions of the analysis models.....	40
Figure 4.3. Tensile stress in the y-direction of the FRP rod( $d=6$ mm): (a) around anchorage of the global model, (b) around the failure section of the sub-model, and (c) in the failure section of the sub-model. ....	44

Figure 4.4. Tensile forces versus element sizes of the FRP rod ( $d=6$ mm).....	46
Figure 4.5. Axial tensile stress distribution in cross-sections of the FRP rod ( $d=6$ mm). .....	47
Figure 4.6. Distribution of axial tensile stress on the failure sections: (a) separated curves of diameters; (b) combined presentation based on the D8 curve. ....	48
Figure 4.7. Tensile strength decrease versus diameter.....	49
Figure 4.8. Axial tensile stress distribution in cross-sections of the FRP rod ( $d=6$ mm) - model B. ....	52
Figure 4.9. Axial tensile stress distribution in cross-sections of the FRP rod ( $d=6$ mm) - model C. ....	53
Figure 4.10. Numerical model of FRP rods with partially-bonding strength. ....	54
Figure 4.11. Typical pull-out failure of FRP rods.....	56
Figure 4.12. Typical failure modes of GFRP and CFRP rods. ....	57
Figure 4.13. Typical failure modes of BFRP rods [87]. ....	58
Figure 4.14. Failure modes of the AFRP rod D6-70-2. ....	64
Figure 4.15. Longitudinal tensile stress distribution in cross-sections of AFRP rod D6-70-2. ....	67
Figure 4.16. Stress distribution in FRP rods with various diameters.....	68
Figure 4.17. Effect of the shear-lag in various AFRP rods.....	69
Figure 5.1. Tensile stress at failure sections of models A, B, and C (D6).....	71
Figure 5.2. Shear-lag effect between the full-bonding and partially-bonding strength (D6)...	72
Figure 5.3. Tensile strength reduction with the diameter. ....	73

## List of tables

Table 1. Properties of Technora fibers and a matrix [36].	29
Table 2. Engineering constants of the AFRP materials.	31
Table 3. CZM parameters for modes I and II in the RVE-2 model simulation.	32
Table 4. Failure criteria of AFRP materials.	33
Table 5. Epoxy and steel tube properties in the analysis models.	37
Table 6. Sizes of the analysis model [45].	37
Table 7. Element sizes and ultimate tensile force results of model (A).	41
Table 8. Tensile stress of each layer in the failure section in the model (A)-D6.	41
Table 9. Comparison of specified, experimental, and predicted results	50
Table 10. Predicted results of AFRP rods.	59
Table 11. Comparison of results.	65

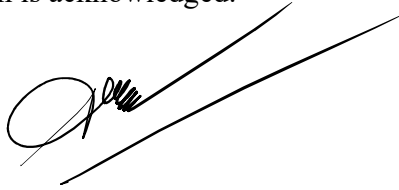
## List of Abbreviations

FRP	Fiber-reinforced polymer
2D	Two dimensional
3D	Three dimensional
RVE	Representative volume element
CZM	Cohesive zone model
AFRP	Aramid fiber-reinforced polymer
UD	Unidirectional
D	Diameter
FC	Failure criterion
CFRP	Carbon fiber-reinforced polymer
NSM	Near surface mounted
ACI	American Concrete Institute
FE	Finite element
FEM	Finite element method
ASTM	American Society for Testing and Materials

## Statement of Original Authorship

‘I hereby declare that this submission is my own work, and to the best of my knowledge, it contains no materials previously published or written by another person, or substantial proportions of material which have been accepted for the award of any other degree or diploma at Yamaguchi University or any other educational institution. Any contribution made to the research by others with whom I have worked at Yamaguchi University or elsewhere is explicitly acknowledged in the thesis. I also declare that the intellectual content of this thesis is the product of my own work, except to the extent that assistance from others in the project's design and conception or style, presentation, and linguistic expression is acknowledged.’

Signature: VO VAN NAM

A handwritten signature in black ink, appearing to read 'VO VAN NAM', is written over a long, thin diagonal line that extends from the top right towards the bottom left.

Date: 2022/02/12.

## Acknowledgments

I would like to thank the following people, without whom I would not have been able to complete my research!

First of all, I would like to express my sincere gratitude to my supervisor, **Prof. Isamu Yoshitake**, Professor of Yamaguchi University, for his supervision, guidance, and encouragement throughout my Ph.D. course. He gave me advice, skills, and comfortable conditions in doing research. I got a lot of obstacles and challenges with my study. However, the encouragement and enthusiasm of **Prof. Isamu Yoshitake** helped me overcome difficulties and complete my research. I have learned many skills from him, such as writing academic papers, conducting research, managing the laboratory. This research work would not be possible without his stimulation, inspiration, and support.

I would like to thank my friend, **Dr. Sy-Ngoc Nguyen**, for his contribution to my study. He also gave me a lot of helpful recommendations in conducting and writing my academic papers.

I would also like to thank the examination committee members for spending their time to assess my doctoral dissertation, including inspectors: **Prof. Hideaki Nakamura**, **Prof. Junji Ohgi**, **Assoc. Prof. Shinichiro Nakashima**, **Assoc. Prof. Azizul Moqsud**, for helpful comments, encouragement, and questions that upgrade my research.

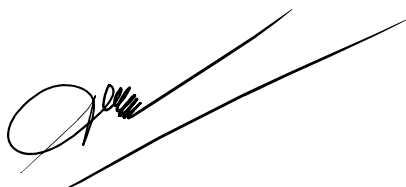
I would like to thank all of Yoshitake's lab members for supporting me from the first day I came to Japan. Especially, I would also like to thank **Dr. Hu Liangjun**, **Mr. Takayuki Makihara**, and my tutor **Mr. Yoshiki Onari**.

I would like to thank **Ms. Tomoko Asano**, the International student support office of Yamaguchi University, for her help in my life. She supported me in renting a house, finding a school for my son, and solving all Japanese policy and law documents.

I would like to thank **Yamaguchi University, International Cooperation Department (Vietnam Ministry of Education and Training)**, **Mien Trung University of Civil Engineering (Vietnam Ministry of Construction)** for supporting my scholarship and advantage conditions for my doctoral course. I also want to thank my co-workers in the Faculty of Civil Engineering. They helped me to complete my teaching mission.

Finally, my warm and heartfelt thanks go to my family for the support and hope they had given to me. Especially, I would like to thank my wife and son, partners of my journey. Thank you all for the strength you gave me.

Date: 2022/02/12.

A handwritten signature in black ink, consisting of a large, stylized initial 'Q' followed by several loops and a long, sweeping horizontal stroke extending to the right.



## Chapter 1. Introduction

### 1.1. Background

Fiber-reinforced polymer (FRP) materials are the combinations of fibers (e.g., carbon, glass, aramid, basalt,...) with matrix materials such as epoxies or vinyl esters. FRPs have been widely used in various engineering applications. Figure 1.1 shows the global market and applications of FRPs, with about 21% for construction [1]. The applications in civil engineer include three main areas: 1) replacing the role of traditional materials (steel, concrete, wood,...) in the structural design; 2) combining with traditional materials in design new structures; 3) strengthening current structures.

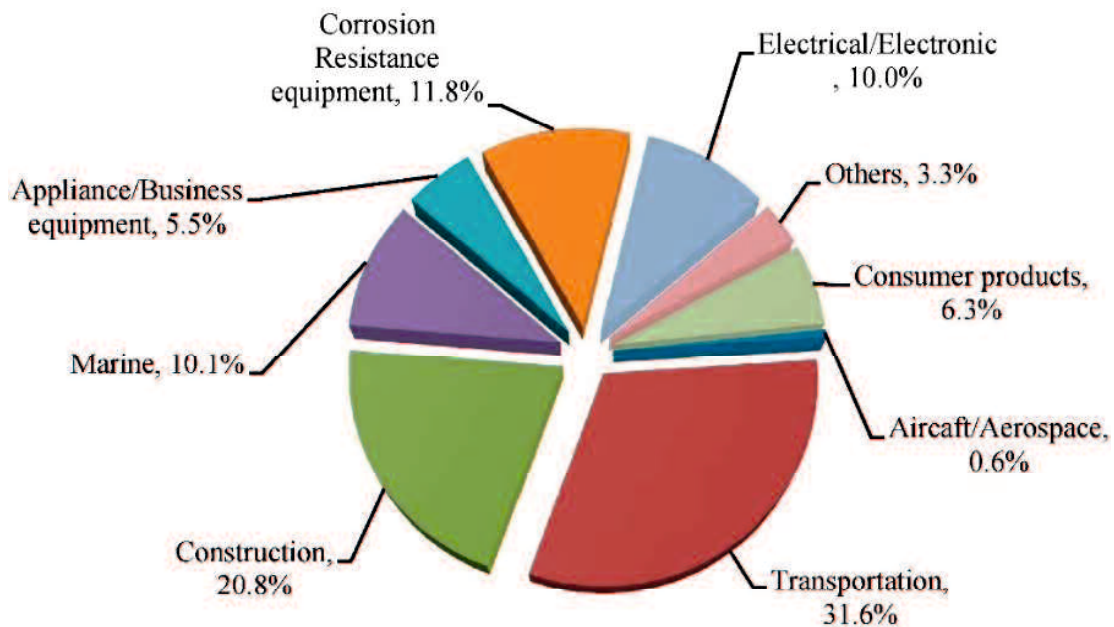


Figure 1.1. Markets and applications of FRP materials [1].

In reinforced-structure applications, three common shapes of the FRPs offered by manufacturers are sheets, cables (tendons), and rods [2]. Four well-known fabricating processes of FRP in civil engineering are filament winding, pultrusion, vacuum compaction processes, matched mold processes. The pultrusion process is the most simple method used in producing rods, tendons, and sheets with unlimited length. Figure 1.2 shows the processes of a pultrusion method.

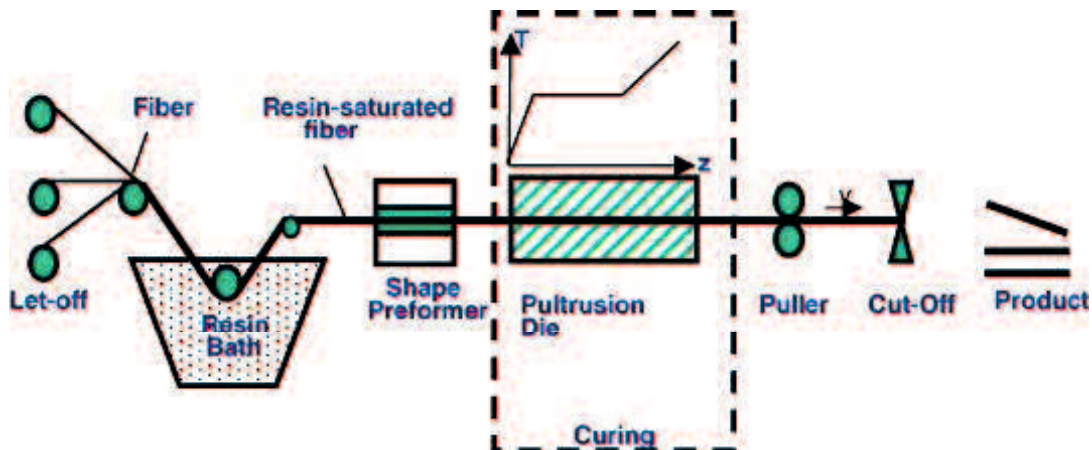


Figure 1.2. Pultrusion method [3].

Most FRPs show higher tensile strength and lower Young's modulus than conventional steel. In steel structures, the FRPs are often used for strengthening steel structures. The common shape of FRP in this strengthening system is sheets (strips). Zhao *et al.* [4] showed bond tests and applications of FRP sheets for strengthening steel hollow section members. Schnerch [5] proposed a guide to design strengthening systems on steel structures. Moreover, the effectiveness FRPs in steel structures was studied under fatigue and instability conditions [6–8].

The applications of FRPs in concrete structures are more popular than those in steel structures. All three FRP shapes (sheet, bar, and tendon) are used in concrete structures. The FRP tendons could play the role of steel cables in the prestressed systems [9–13]. The FRP bars are used as steel rebars in concrete structures or as strengthening materials in near-surface mounted (NSM) systems [14–24]. The FRP plates are generally used in externally bonded systems [25–30]. The design of concrete structures strengthened with FRP materials has been guided in some codes such as ACI PRC-440.1-15 [31], CEB-FIP 40 [32], and ACI 440.2R-08 [33].

The FRP bars are more popular than the other shapes. FRP bars include many shapes of the cross-sections, as shown in Figure 1.3. The general shape of the FRP bars is the round section called FRP rods. The shape of FRP rods is similar to that of steel rebars. In engineering structures, FRP rods are often used to enhance the load-carrying capacity of concrete structures subjected to tensile shear forces or bending moments. Hence, the load-capacity of FRP rods under tension is a significant factor. Moreover, the tensile behavior of the FRP rods needs to be studied in detail.



Figure 1.3. Pultrussion FRP bars [19].

## 1.2. Research objectives

The properties of FRP rods depend on the quality of constituting materials, fiber orientation, and volume fraction. The matrix in FRP rods shows the isotropic property. However, the fibers in FRP rods present various properties, such as the isotropic behavior (glass fibers) and transversely isotropic behavior (carbon and aramid fibers). Many tests on FRP rods made of a similar fiber volume fraction showed that the apparent tensile strength decreases with the diameter increase [34–36]. Some studies [37–43] indicated that the shear-lag effect reduces the tensile strength of FRP rods. It is due to the fact that the shear-lag causes unequal tensile stress distribution on the cross-section, with higher values at outer and lower ones at inner areas. However, a reasonable procedure for predicting the axial tensile stress distribution in the cross-section has not been proposed yet. The stress distribution is a factor to assess the failure of FRP rods. In addition, it is unclear how the transversely isotropic properties of FRP rods and such fibers (aramid and carbon) are collected and evaluated. Consequently, the behavior of FRP rods in the tensile models has been limited.

A numerical model of the FRP rods under tension was suggested for the bonded anchorage carbon FRP tendons [44]. However, this study only focused on analyzing the bond performance of the filling material. In addition, it is inappropriate to assume carbon FRP rods as isotropic materials. It should be noted that FRP rods could directly connect to concrete or via an adhesive. Therefore, in general, the tensile behavior of FRP rods depends on many factors, such as FRP materials, adhesives, and bond interfaces. To quantify the failure of FRP rods in detail, the present study employed two three-dimensional (3D) models of FRP rods under tensile forces. The first numerical model of the FRP rod assumed the full-bonding at the interface between FRP rods and the filling material [45]. The second numerical model considered the effect of the interfaces (FRP rod-epoxy and epoxy-steel tube) on the failure of FRP rods.

### **1.3. Scopes of the research**

The study aims to demonstrate the failure properties of FRP rods under various potential conditions. Two finite element (FE) models for a tensile test of the FRP rod in a bond joint were developed. The reference fiber material is aramid FRP (AFRP). The AFRP rod is embedded at the center of the steel tube filled with a high-performance epoxy resin. The properties of interfaces (FRP rod-epoxy and epoxy-steel tube) are varied to evaluate the interfacial bonding effect. A technique called the sub-modeling method was used to enhance the accuracy of the results. Furthermore, the study proposes representative volume element (RVE) models to predict the mechanical properties and failure criteria of the FRP material. The effect of transversely isotropic properties of fibers on the stiffness of FRP rods was considered in RVE models. Finally, the FE models are applied to various diameters (3, 4, 6, and 8 mm) to quantify the diameter effect. The relationship of failure modes, the shear-lag effect, and the load-capacity of FRP rods is illustrated in detail. The following issues are addressed in detail:

1. The transversely isotropic properties of FRP rods from original materials were determined by using RVE models.

2. The failure criteria of the FRP material were estimated to assess the failure of FRP rods.

3. Two models (full-bonding strength and partially-bonding strength) relating to the effect of the interfaces were presented to investigate the failure of FRP rods.

4. The relationship of failure modes, the shear-lag effect, and the load-capacity of FRP rods was illustrated in each case of the interfacial bond.

5. The model in this study can be applied to predict the load-capacity of FRP rod in tension.

#### **1.4. Outline**

Chapter 1: This is the introduction section of the knowledge of the tensile behavior of FRP rods. The section also shows the limitations of previous studies and the purpose of the present study. In addition, the chapter shows the scope of the present study and the layout of the thesis.

Chapter 2: This is the literature review of previous researches. The section highlights the gaps in previous studies and proposes models and theories for the present study.

Chapter 3: This chapter shows numerical models to predict the transversely isotropic properties of FRP material. In addition, the failure criteria of the FRP material are determined. The tensile properties of the composite material were investigated in the transverse direction.

Chapter 4: This chapter shows numerical models under tensile forces in two cases of the interfacial bond between FRP rods and filling materials. Two models, A and B, were proposed to investigate the fiber effect on the composite properties. The failure modes and shear-lag effects of FRP rods were studied in detail.

Chapter 5: This chapter shows the discussion about the fiber-properties effects and the bond effects on the longitudinal tensile properties of FRP rods. The shear-lag effect was compared in two cases of the interfacial bond between the FRP rod and filling material.

Chapter 6: This chapter summarized the significant findings and gave a final judgment on them. In addition, the chapter suggests future works and limitations.

## Chapter 2. Literature review

The properties of FRP rods depend on the quality of constituting materials, fiber orientation, and fiber volume fraction. Modeling all fibers and the matrix in a composite structure is a challenge due to the small sizes of fibers. A simple rule is to consider heterogeneous materials as equivalent homogeneous materials with approximate mechanical properties, as shown in

Figure 2.1. FRP rods are unidirectional (UD) fiber-reinforced composites. Therefore, the FRP rods show properties of transversely isotropic materials. Prediction of engineering elastic constants helps to assess the FRP rod behaviors under tensile loading. Moreover, the strength of FRP materials should be considered in the failure of FRP rods.

The properties of interfaces (FRP rod-epoxy and epoxy-steel tube) are varied to evaluate the interfacial bonding effects. The interfaces are modeled as cohesive zone models in case of partially-bonding strength. The accuracy of results was enhanced by modeling the FRP rods with finer meshes. The sub-modeling method was applied to interpolate the boundary conditions of FRP rod models from the entire models of tensile tests.

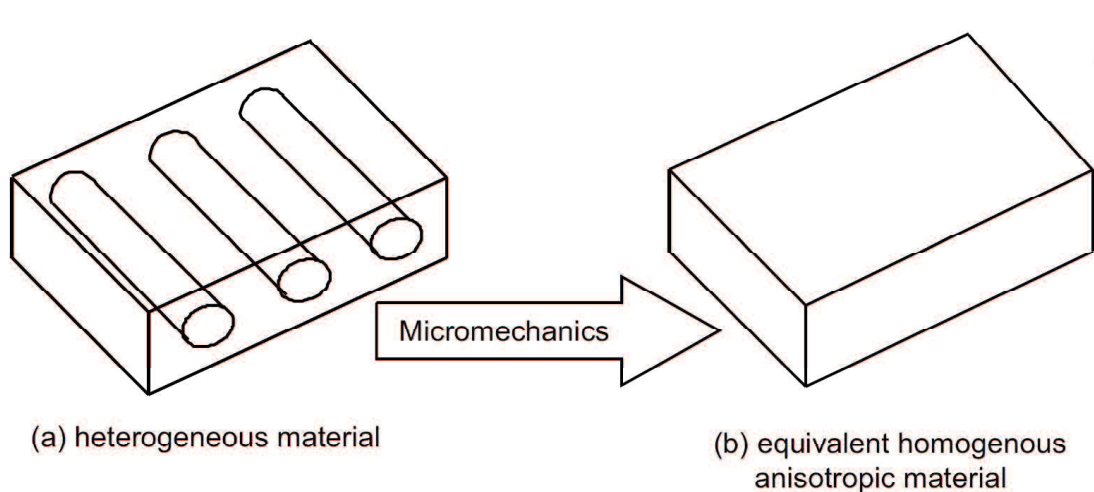


Figure 2.1. Micromechanics process [46].

## 2.1. Determining properties of FRP rods

Figure 2.2 shows the tensile properties of fibers, a matrix, and their composition. The tensile strengths of the fibers are significantly higher than that of the matrix. However, the ultimate tensile strain of the matrix is much higher than that of the fibers. The failure strain of an FRP composite is assumed to be the ultimate strain of fibers.

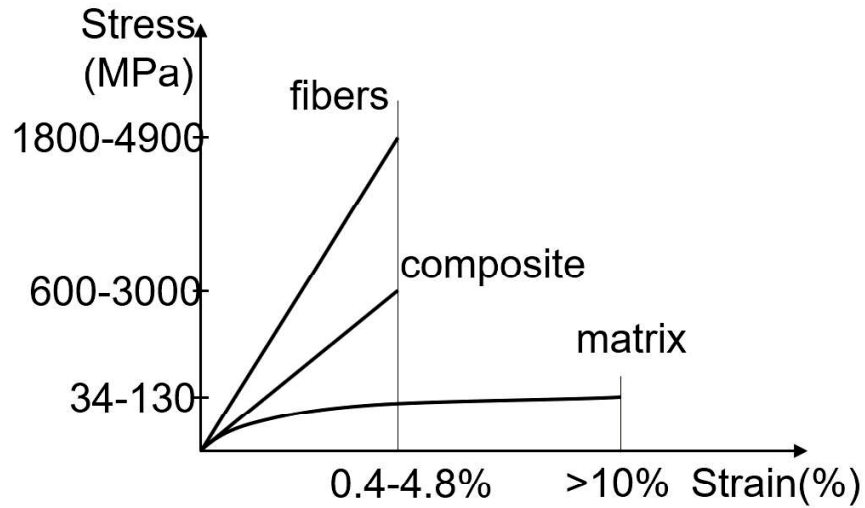


Figure 2.2. Stress-strain relationships of fibrous reinforcement and matrix [47].

This study focused on AFRP rods made of unidirectional fibers and a matrix by the pultrusion method. Both AFRP rods and aramid fibers exhibit transversely isotropic properties. The transversely isotropic material follows restrictions on engineering constants in Eq. (1). Hook's law of the transversely isotropic materials was introduced in Equation (1)

$$\begin{Bmatrix} \sigma_1 \\ \sigma_2 \\ \sigma_3 \\ \sigma_4 \\ \sigma_5 \\ \sigma_6 \end{Bmatrix} = \begin{bmatrix} C_{11} & C_{12} & C_{12} & 0 & 0 & 0 \\ C_{12} & C_{22} & C_{23} & 0 & 0 & 0 \\ C_{12} & C_{23} & C_{22} & 0 & 0 & 0 \\ 0 & 0 & 0 & (C_{22} - C_{23})/2 & 0 & 0 \\ 0 & 0 & 0 & 0 & C_{66} & 0 \\ 0 & 0 & 0 & 0 & 0 & C_{66} \end{bmatrix} \begin{Bmatrix} \varepsilon_1 \\ \varepsilon_2 \\ \varepsilon_3 \\ \gamma_4 \\ \gamma_5 \\ \gamma_6 \end{Bmatrix} \quad (1)$$

Engineering elastic constants include Young's moduli ( $E_1, E_2, E_3$ ), shear moduli ( $G_{12}, G_{13}, G_{23}$ ), and Poisson's ratios ( $\nu_{12}, \nu_{13}, \nu_{21}, \nu_{31}, \nu_{23}, \nu_{32}$ ). The relations between parameters follow Equation (2). The number 1 denotes the longitudinal direction of the fibers. The numbers 2 and 3 indicate the transverse direction.

$$\begin{aligned} E_2 &= E_3 \\ G_{12} &= E_{13} \\ \nu_{12} &= \nu_{13} \\ G_{23} &= \frac{E_2}{2(1 + \nu_{23})} \end{aligned} \quad (2)$$

The transversely isotropic material follows restrictions on engineering constants in Equation (3).

$$\begin{aligned} \frac{\nu_{ij}}{E_i} &= \frac{\nu_{ji}}{E_j} \\ 0 < \nu_{ij} &< \sqrt{\frac{E_i}{E_j}}; \quad i, j = 1..3; i \neq j \\ \Delta = 1 - \nu_{12} \nu_{21} - \nu_{23} \nu_{32} - \nu_{31} \nu_{13} - 2 \nu_{21} \nu_{32} \nu_{13} &> 0 \end{aligned} \quad (3)$$

Experiments to examine the properties of FRP materials are always a big challenge due to the small sizes of fibers. To determine the properties of FRP material, all engineering constants have to be predicted to define each value  $C_{ij}$  in Equation (1). Many methods could be applied to find engineering constants and listed in two groups: the rule of mixture formulas and numerical models. The theory of the prediction methods is based on the analysis of micromechanics using the representative volume elements (RVEs). The shape of an RVE model depends on the fiber volume fraction and fiber distribution, as shown in Figure 2.3.

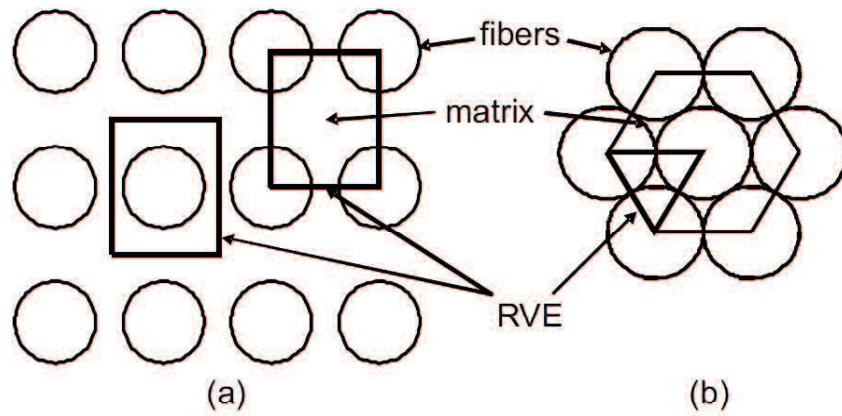


Figure 2.3. Typical representative volume elements (RVE) for (a) rectangular packing array and (b) hexagonal packing array [46].

### 2.1.1. Methods based on the rule of mixture formulas

This method assumes fibers and the matrix as isotropic materials in the RVE model. Figure 2.4 shows an RVE model under tension in the longitudinal direction. The model assumes a perfect bond between fibers and the matrix.

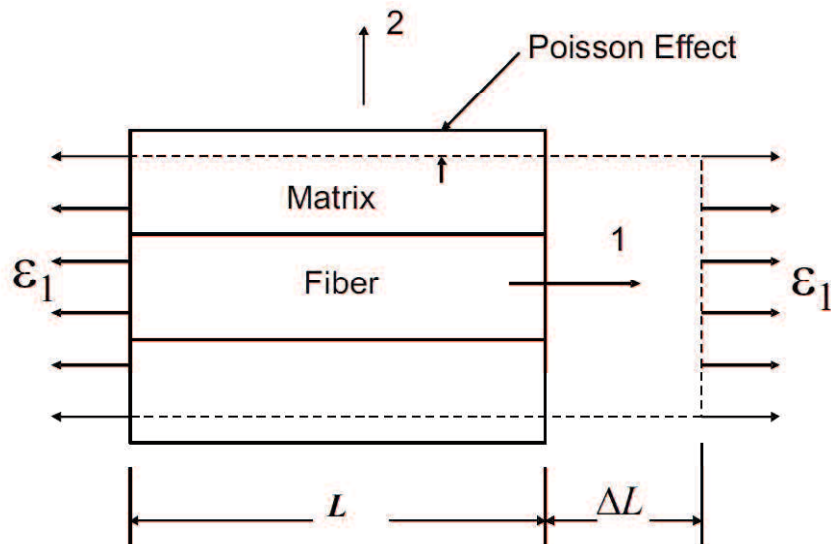


Figure 2.4. RVE subjected to longitudinal uniform strain [46].

Barbero [46] presented Equation (4) to calculate the longitudinal modulus  $E_1$ . The equation follows the rule of mixtures with fiber ratio  $V_f$  and matrix ratio  $V_m$ . The

longitudinal modulus  $E_1$  was estimated from the modulus of fibers  $E_f$  and modulus of matrix  $E_m$ . The value  $E_m$  is much lower than  $E_f$ . It means that the longitudinal modulus mainly depend on the modulus of fibers.

$$E_1 = E_f V_f + E_m V_m \quad (4)$$

The transverse modulus is predicted from the RVE model under transverse tension, as shown in Figure 2.5. Equation (5) was used to find the transverse modulus. However, this equation underestimated the actual value of the transverse modulus  $E_2$ . Barbero [46] indicated that the Equation (5) should not be utilized for designing composite structures.

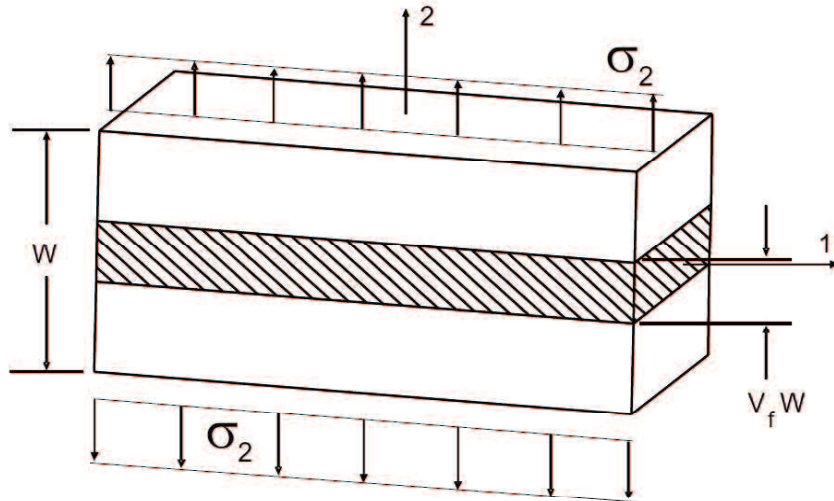


Figure 2.5. RVE subjected to transverse uniform stress [46].

$$E_2 = \frac{E_f E_m}{E_f V_m + E_m V_f} \quad (5)$$

Halpin-Tsai [48] proposed a better equation as follow:

$$E_2 = E_m \left[ \frac{1 + \zeta \eta V_f}{1 - \eta V_f} \right] \quad (6)$$

$$\eta = \frac{(E_f/E_m) - 1}{(E_f/E_m) + \zeta}$$

where  $\zeta$  is an empirical parameter. However, it is quite complicated to determine the value  $\zeta$ .

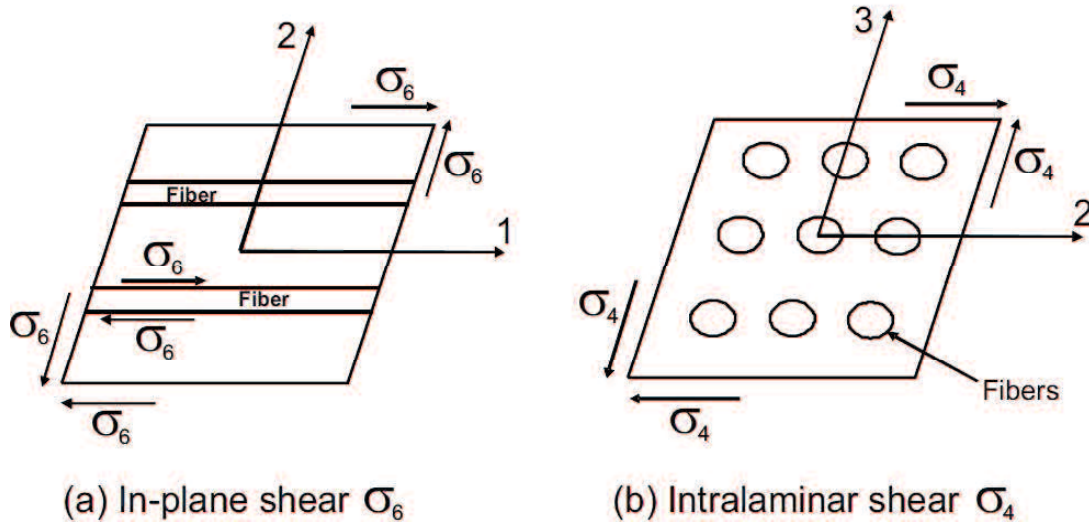


Figure 2.6. Models to determine the shear moduli [46].

The shear moduli include the in-plane shear and intralaminar shear, as shown in

Figure 2.6. The prediction of in-plane shear modulus follows Equation (7) [46]. Equation (7) based fiber-matrix volume fraction is quite simple. However, it is not an accurate equation.

$$G_{12} = G_{13} = \frac{G_m}{V_m + V_f G_m / G_f} \quad (7)$$

Barbero [46] presented a much accurate equation for in-plane shear modulus and intralaminar shear modulus, as follows:

$$\begin{aligned}
G_{12} = G_{13} &= G_m \left[ 1 + \frac{V_f(1 - G_m/G_f)}{G_m/G_f + S_3(1 + V_f)(1 - G_m/G_f)} \right] \\
S_3 &= 0.49247 - 0.47603V_f - 0.02748V_f^2 \\
G_{23} &= G_m \frac{V_f + \eta_4(1 - V_f)}{\eta_4(1 - V_f) + V_f G_m/G_f} \\
\eta_4 &= \frac{3 - 4\nu_m + G_m/G_f}{4(1 - \nu_m)}
\end{aligned} \tag{8}$$

Predicting the Poisson ratios from an RVE model is a big challenge. Barbero [46] showed a simple equation based on the rule of mixtures. The in-plane Poisson ratio was calculated as follows:

$$\nu_{12} = \nu_{13} = \nu_f V_f + \nu_m V_m \tag{9}$$

All equations introduced above are the most simple method to predict the engineer constants of an equivalent homogeneous material from an RVE model. However, Barbero [46] did not show an equation to find the Poisson ratio  $\nu_{23}$ . Another method uses the periodic microstructure model (PMM). Barbero [46,49] indicated that this method could predict all engineering constants of the transversely isotropic material. The predicted results using the PMM method fit experimental results in the cases of isotropic fibers, such as glass and basalt. However, this method is unsuitable for applying to composites of transversely isotropic fibers, such as carbon and aramid.

### 2.1.2. Methods based on the numerical models

RVE modeling is an effective method to find the mechanical properties. Sun and Vaidya [50] employed two numerical RVE models based on the hypothesis of the square and hexagonal distributions of fibers, as shown in Figure 2.7. The method in this study was compared with methods using the energy balance approach [51] and the mechanical approach [51-52]. The results demonstrated that RVE model methods are more effective than predicting engineering constants of unidirectional (UD) FRP materials.

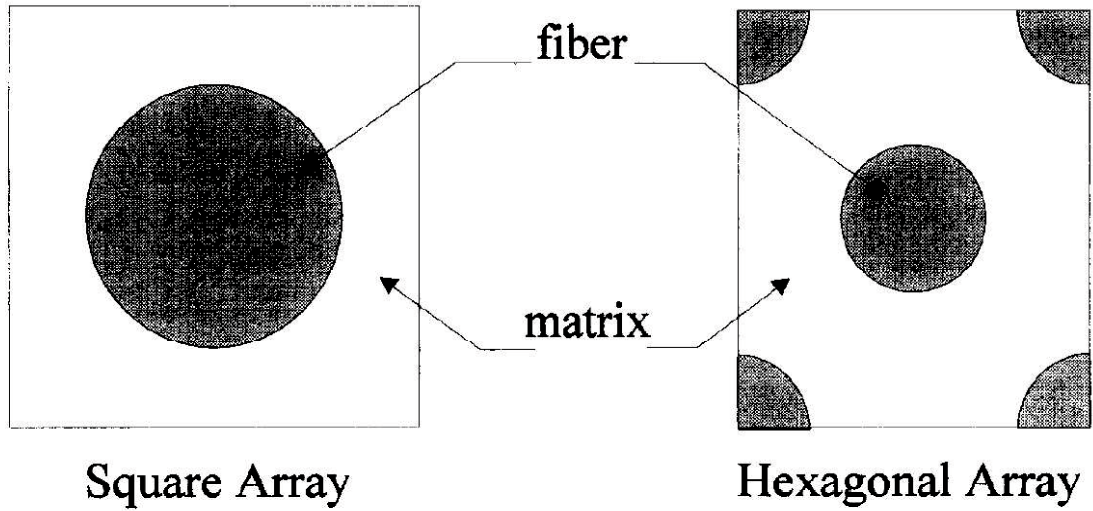


Figure 2.7. RVE models of square and hexagonal array distributions [50].

Barbero [49] employed a hexagonal RVE model into ANSYS software [54] to predict the FRP material properties. Figure 2.8 shows the details and sizes of the RVE model. The interfaces between fibers and the matrix are perfect. The material properties of fibers and matrix are assumed as linear. Equation (10) shows the relationship between the three-dimension (3D) sizes of an RVE model.

$$\begin{aligned}
 a_1 &= a_2/4 \\
 a_3 &= a_2 \tan(60^\circ) \\
 V_f &= \frac{\pi d_f^2 / 2}{2a_2 2a_3}
 \end{aligned} \tag{10}$$

The basic theory of this method is using the averaging method. The relationship between average stress-strain in the RVE-1 model is assumed as follow:

$$\bar{\sigma}_\alpha = C_{\alpha\beta} \bar{\varepsilon}_\beta \tag{11}$$

where  $\bar{\sigma}_\alpha$  and  $\bar{\varepsilon}_\beta$  are the average stress and strain, respectively. Values are calculated over the total volume of the RVE model. The coefficients ( $\alpha, \beta = 1-6$ ) are contracted notation to indicate six following components of stress and strain.  $C_{\alpha\beta}$  is the stiffness tensor members in Equation (1).

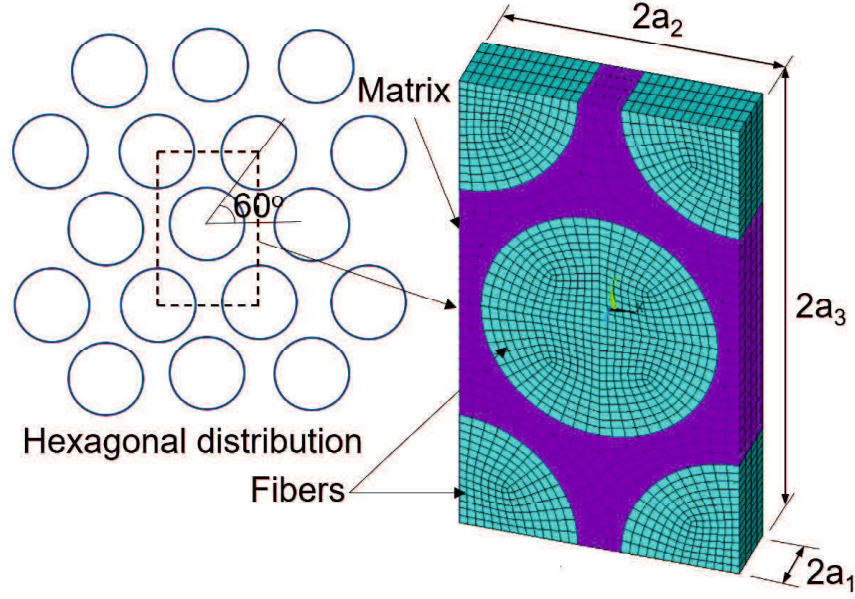


Figure 2.8. Hexagonal array RVE model.

Luciano *et al.* [55] demonstrated the relationship between displacements of edges and strains of the RVE model, as shown in Equation (12).

$$\begin{aligned}
 u_i(a_1, x_2, x_3) - u_i(-a_1, x_2, x_3) &= 2a_1 \varepsilon_{i1}^0 & \begin{cases} -a_2 \leq x_2 \leq a_2 \\ -a_3 \leq x_3 \leq a_3 \end{cases} \\
 u_i(x_1, a_2, x_3) - u_i(x_1, -a_2, x_3) &= 2a_2 \varepsilon_{i2}^0 & \begin{cases} -a_1 \leq x_1 \leq a_1 \\ -a_3 \leq x_3 \leq a_3 \end{cases} \\
 u_i(x_1, x_2, a_3) - u_i(x_1, x_2, -a_3) &= 2a_3 \varepsilon_{i3}^0 & \begin{cases} -a_1 \leq x_1 \leq a_1 \\ -a_2 \leq x_2 \leq a_2 \end{cases}
 \end{aligned} \tag{12}$$

where  $u_i$  and  $\varepsilon_{ij}^0$  are the applied displacement on each edge and applied strain of the RVE model, respectively. In addition,  $2a_j \varepsilon_{ij}^0$  indicates the total displacement over length  $2a_j$  to enforce a strain  $\varepsilon_{ij}^0$ .

The theory assumes continuity inside the RVE model. It means that there are no voids and cracks. The applied strain  $\varepsilon_{ij}^0$  denotes the average strain of volume  $\bar{\varepsilon}_\beta$ :

$$\bar{\varepsilon}_{ij} = \frac{1}{V} \int_V \varepsilon_{ij} dV = \varepsilon_{ij}^0 = \bar{\varepsilon}_\beta \tag{13}$$

where  $i, j = 1-3$  is contracted notation. The relationship between  $i, j$  and  $\alpha, \beta$  follows the rule in Equation (14):

$$\begin{aligned} \alpha, \beta = i & & \text{if } i = j \\ \alpha, \beta = 9 - i - j & & \text{if } i \neq j \end{aligned} \quad (14)$$

By setting a unit value for the applied strain in Equation (11) with  $\beta = 1-6$ , the RVE model is subjected to six components of strain. The computation is conducted with each of the cases. The stiffness tensor  $C_{\alpha\beta}$  could be determined from Equation (15).

$$C_{\alpha\beta} = \bar{\sigma}_\alpha = \frac{1}{V} \int_V \sigma_\alpha(x_1, x_2, x_3) dV \text{ with } \bar{\epsilon}_\beta = 1 \quad (15)$$

Barbero [49] reported a numerical simulation of the RVE model in ANSYS to find all components of the stiffness tensor  $C_{\alpha\beta}$ . In addition, the study showed a procedure for calculating all engineering constants of the transversely isotropic material via tensor components in Equation (16):

$$\begin{aligned} E_1 &= C_{11} - 2C_{12}^2 / (C_{22} + C_{23}) \\ E_2 = E_3 &= [C_{11}(C_{22} + C_{23}) - 2C_{12}^2] (C_{22} - C_{23}) / (C_{11}C_{22} - C_{12}^2) \\ G_{12} &= G_{13} = C_{66} \\ G_{23} &= C_{44} = (C_{22} - C_{23}) / 2 \\ \nu_{12} &= \nu_{13} = C_{12} / (C_{22} + C_{23}) \\ \nu_{23} &= (C_{11}C_{23} - C_{12}^2) / (C_{11}C_{22} - C_{12}^2) \end{aligned} \quad (16)$$

where  $E$ ,  $G$ , and  $\nu$  denote Young's modulus, shear modulus, and Poisson's ratio, respectively. The index numbers in these notations include 1 for the longitudinal direction of fibers, 2 and 3 for transverse directions of fibers, respectively.

A significant advantage of this method is simple for calculation. Although the formulae are currently more popular for predicting engineering constants in composite practice designs, the methods are less accurate than the numerical RVE model methods. In addition, the second advantage of using computer simulations is that it allows investigation for various cases of fibers, such as isotropic or transversely isotropic properties. Therefore, the numerical RVE model methods adapt the properties of aramid

composites in this study. The present study enhanced the RVE model developed by Barbero [49] with transversely isotropic properties of fibers. The model was named RVE-1 used in predicting engineering constants of FRP rods.

## 2.2. Failure criterion and strengths of FRP materials

The application of failure criteria for predicting damage of UD composites is complicated due to complex failure behavior. Cui *et al.* [56] compared many stress-based criteria in predicting delamination. The stress-based criteria include interactive criteria (Tsai-Hill [57], Tsai-Wu [58], and Hashin-Rotem [59,60]) and non-interactive criteria (the maximum stress and strain criteria). Cui *et al.* [56] showed that the interactive criteria are better than the non-interactive criteria. However, these criteria are based on the combination of various stresses. Therefore, it is difficult to use the interactive criteria for predicting failure modes.

The fiber angle formed by fibers and force directions is an important factor affecting the utilization of criteria. Vasiliev and Morozov [61] indicated that the maximum stress criterion is consistent with experimental results when the fiber angle is close to 0° and 90°. With respect to the fibers angle 0° in the present study, the maximum stress criterion was employed to predict the failure of FRP rods. Furthermore, the advantage of the maximum stress criterion is able to identify failure modes which the interactive criterion can not do.

The ratio between stress and strength was calculated in each direction, which is shown in Equation (17). As specified in the FRP rod models, three axes include 1 fiber direction, 2 radius direction, and 3 rotation angle  $\alpha$  direction. The failure index is the maximum value of stress-strength ratios. The failure will occur when the failure index  $I_F = 1$ .

$$I_F = \max \begin{cases} F_{1c}/F_{1cf} \text{ or } F_{1t}/F_{1tf} \\ F_{2c}/F_{2cf} \text{ or } F_{2t}/F_{2tf} \\ F_{3c}/F_{3cf} \text{ or } F_{3t}/F_{3tf} \\ |F_{12}|/F_{12f} \\ |F_{13}|/F_{13f} \\ |F_{23}|/F_{23f} \end{cases} \quad (17)$$

where  $I_F$  is the failure index.  $F_{1c}, F_{2c}, F_{3c}$  denote the compressive stress in three directions.  $F_{1t}, F_{2t}, F_{3t}$  denote the tensile stress in three directions. The other notations denote strengths in 3D models.

Strength is determined when failure initially occurs in structures. Therefore, strength is one of the criteria to assess the damage in structures. The strength of composite structures is more complicated than that of traditional materials like steel and aluminum. There are a variety of failure modes, including fiber breaking, matrix crazing, fiber-matrix interface debonding, delamination, ...[46]. Determining strength values in Equation (17) helps to identify the failure of FRP materials. The present study investigated the tensile behavior of FRP rods. Therefore, the authors focused on the tensile strength ( $F_{1tf}, F_{2tf}, F_{3tf}$ ) and shear strength ( $F_{12f}, F_{13f}, F_{23f}$ ).

### 2.2.1. Prediction strengths by formulas

Determining all strength values in Equation (17) is difficult. It requires a lot of information about fibers and the matrix in the composite. Barbero [46] introduced the longitudinal tensile strength  $F_{1tf}$  and transverse tensile strength  $F_{2tf}$  of UD composites in Equations (18) and (19), respectively.

$$F_{1tf} = F_{ft}V_f + \sigma_m^*(1 - V_f)$$

$$\sigma_m^* = F_{ft} \frac{E_m}{E_f} \quad (18)$$

where  $F_{ft}$  is the tensile strength of the fibers.  $\sigma_m^*$  is the stress of the matrix at failure time.  $E_m$  and  $E_f$  are moduli of the matrix and fibers, respectively.

$$F_{2tf} = F_{mt}C_v \left[ 1 + (V_f - \sqrt{V_f}) \left( 1 - \frac{E_m}{E_f} \right) \right]$$

$$C_v = 1 - \sqrt{\frac{4V_v}{\pi(1 - V_f)}} \quad (19)$$

where  $F_{mt}$  is tensile strength of the matrix.  $E_T$  is the transverse modulus of the fibers.  $V_v$  is the void volume fraction in composite.  $C_v$  is an empirical parameter. Therefore, the proper value of  $C_v$  is unclear in the calculation.

Transverse strength also could be followed Equation (20) based on the transverse modulus of the composite  $E_2$  [46].

$$F_{2tf} = F_{mt}C_v(1 - V_f^{1/3})\frac{E_2}{E_m} \quad (20)$$

The in-plane shear strength of UD composites was determined as follows

$$F_{12f} = F_{13f} = F_{mt}C_v(1 + (V_f - \sqrt{V_f}))\left(1 - \frac{G_m}{G_A}\right) \quad (21)$$

where  $G_m$  and  $G_A$  are the shear modulus of the matrix and the axial shear modulus of the fibers, respectively.

The transverse shear strength  $F_{23f}$  was determined from the Mohr-Coulomb criterion for UD composites under the transverse compression.

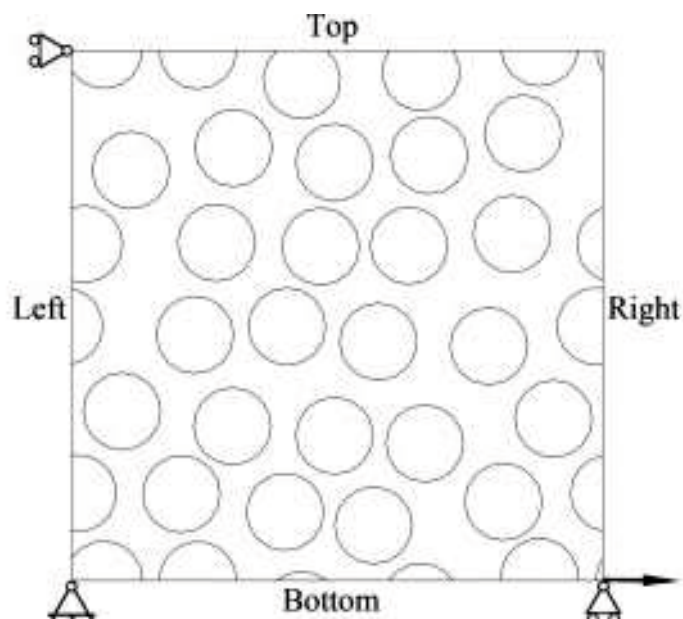
$$F_{23f} = F_{2cf}\cos\alpha_0(\sin\alpha_0 + \cos\alpha_0\cot 2\alpha_0) \quad (22)$$

where  $F_{23f}$  is the transverse compressive strength of UD composites. Parameter  $\alpha_0$  the angle of the fracture plane.

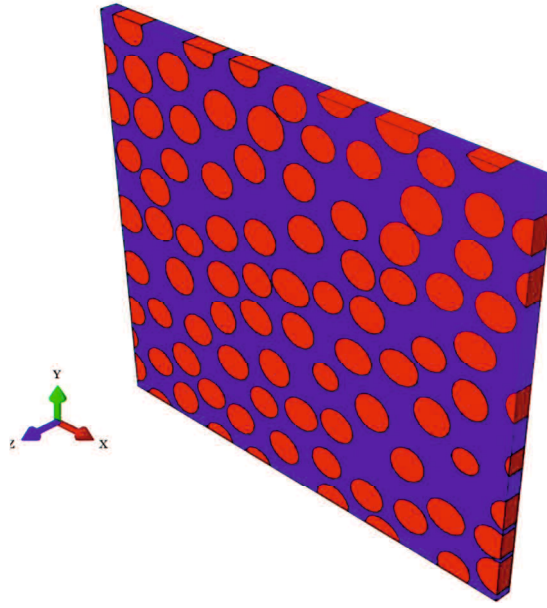
In addition, Barbero [46] introduced some formulas based on the fracture toughness in modes I and II to predict the transverse tensile strength or shear strength. However, these equations are complicated and require experimental values of fracture toughnesses. Predicting the strengths of UD composites by formulas is simple. However, these methods show many disadvantages, especially in predicting transverse tensile strength and shear strength.

### 2.2.2. Prediction strengths by RVE models

The hexagonal RVE model called RVE-1 in Figure 2.8 is inappropriate to predict the strengths of FRP materials while it can be used for assessing other properties of FRP. The primary reason is owing to unequal transverse-strengths in the X and Y directions. Using 3D RVE models to predict the strengths of composite materials has been proposed in some studies [62–66]. Asp *et al.* [62] conducted simulation models based on the fiber distribution, including square array, hexagonal array, and square-diagonal array. The study assumed the matrix as a linear material. In addition, the main weakness of this study is that it ignored the effects of the interfacial bond between fibers and matrix.



(a)



(b)

Figure 2.9. RVE models: (a) 2D model [65], (b) 3D model [66].

Three studies [63–65] suggested the RVE models with the random distribution of fibers. The bilinear CZM was applied to model the interfaces between fibers and matrix. These studies highlighted the significant effect of the interfacial strengths on the transverse strength of the RVE model. In addition, these authors indicated that contact stiffness and interfacial fracture energy slightly affect the transverse tensile strength. These studies assumed that the interfacial strengths ( $\sigma_{max}^n, \sigma_{max}^t$ ) were the same for both modes I and II. The interfacial strengths varied from 15 to 90 MPa [63], 60 to 120 MPa [64], 39.1 to 78.2 MPa [65]. Three previous studies used two-dimensional elements for the numerical models. Such approaches, however, have failed to address the in-plane shear strength of UD composites. Bhuiyan [66] proposed a 3D model to predict failure strengths in UD composites. The study assumed that matrix and interface strengths are similar, with a specified value of 80 MPa. The theory is inappropriate in considering the failure of UD composite under transverse tension, as shown in Figure 2.10. The failure firstly appears at the fiber-matrix interfaces where the normal interfacial strength  $\sigma_{max}^n$  is smaller than matrix tensile strength.

Regarding the interfacial strengths, Yademellat *et al.* [67] and Floros *et al.* [68] showed that the interface strengths were distinct in modes I and II. The interfacial normal strength in these studies was 20 and 8.3 MPa, respectively [63, 64]. Indeed, the interfacial

normal strength was much smaller than the interfacial tangential strength and matrix tensile strength. Hence, the low interfacial normal strength for the RVE-2 model was recommended in the present study.

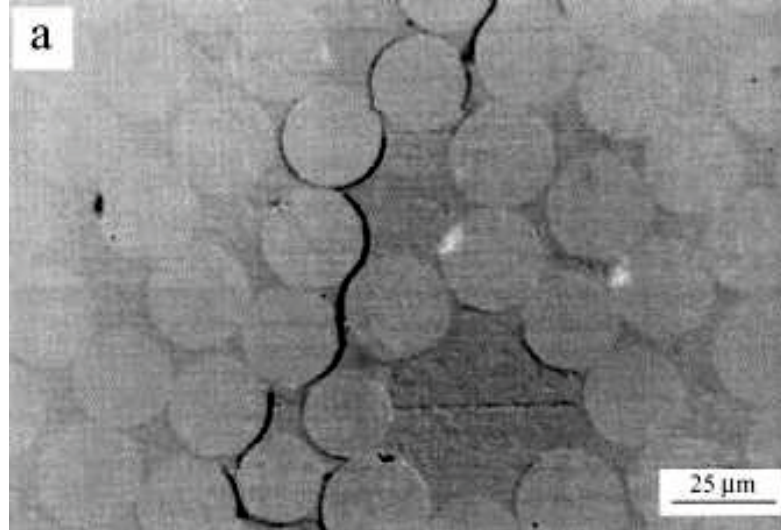


Figure 2.10. Debonding at fiber-matrix interface and failure under transversal load [69].

The present study proposed a new model, RVE-2, to predict the strengths of FRP rod material, as shown in

Figure 2.11. The fiber distribution in the new model was assumed as a random distribution. With respect to the effect of the interfacial normal strength, the present study varied the strength ratio  $R_s$  from 10 to 25% where  $R_s = \sigma_{max}^n / \sigma_{resin}^y$  is the ratio between the interfacial normal strength  $\sigma_{max}^n$  and the tensile strength  $\sigma_{resin}^y$  of the vinyl ester resin. The von Mises yield criterion was employed to predict the tensile strength of the RVE-2 models. The equivalent stress  $\sigma_e$  can be calculated as follow:

$$\sigma_e = \sqrt{\frac{1}{2}[(\sigma_1 - \sigma_2)^2 + (\sigma_2 - \sigma_3)^2 + (\sigma_3 - \sigma_1)^2]} \quad (23)$$

where  $\sigma_1$ ,  $\sigma_2$ , and  $\sigma_3$  are principal stresses of each matrix element.

Furthermore, the displacement was applied on the boundaries of the RVE-2 models in each case to find transverse, longitudinal, and shear strengths. In predicting transverse and shear strengths, the failure occurs when the equivalent stress  $\sigma_e$  reaches the yield stress  $\sigma_{resin}^y$  of the matrix. In predicting longitudinal strength, the failure of the RVE-2 models happens when the fiber strain peaks the ultimate strain of fibers. From this result, the average strength in each case of the RVE-2 models will be calculated by the average theory as follow:

$$\overline{\sigma}_y = \frac{1}{V} \int_V \sigma_i dV = \frac{\sum_i \sigma_i V_i}{V} \quad (24)$$

where  $\overline{\sigma}_y$  is the average strength of the RVE-2 model under an applied displacement.  $\sigma_i$  and  $V_i$  are the stress and volume of the element  $i_{th}$  in the RVE-2 model, respectively.  $V$  is the total volume of the RVE-2 model.

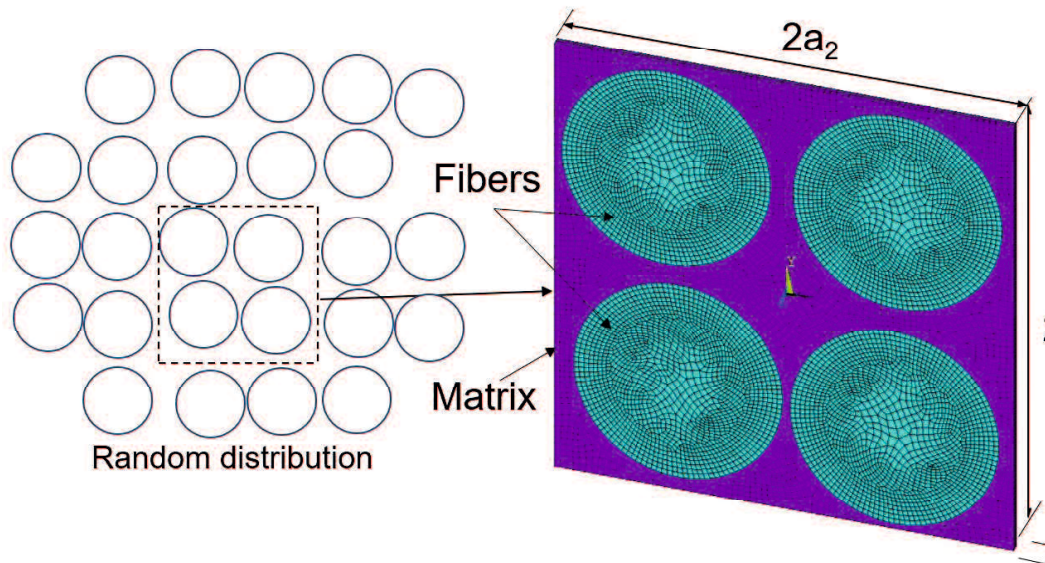


Figure 2.11. Random distribution RVE model (RVE-2).

### 2.3. Cohesive zone model

Cohesive zone model (CZM) is an effective tool to simulate the delamination or crack at an interface. The CZM model is based on the traction separation between contact

stress ( $\sigma$ ) and contact gap ( $u$ ), which is used for both modes I (normal separation) and II (tangential separation) of debonding. Basic CZM models were introduced in ANSYS software [54], including the bilinear behavior model and exponential behavior model.

The exponential model was proposed by Xu and Needleman [70]. This model could be applied to model the interface of each separated mode I or II. The major drawback of this model is that the fracture energy is assumed the same in both modes I and II. The bilinear cohesive zone model (CZM) proposed by Alfano and Crisfield is simpler than the general exponential cohesive law [71]. The bilinear cohesive zone model (CZM) was simulated as contact elements at the interfaces. Figure 2.12 shows the traction separation between contact stress ( $\sigma$ ) and contact gap ( $u$ ), which is used for both modes I (normal separation) and II (tangential separation) of debonding. Each mode needs three parameters such as contact stiffness  $K$ , maximum contact stress  $\sigma_{max}$ , and maximum contact gap  $u_c$  to define the bilinear traction-separation law. Hence, the fracture energy release rate could be calculated via the relationship  $G_c=(\sigma_{max}u_c)/2$ . In this study, the contact CZM model provided by ANSYS was employed with CONTA173 and TARGE170 elements to simulate the interface bonding in two cases: fibers with vinyl ester resin or the FRP rod and steel tube with the filling material).

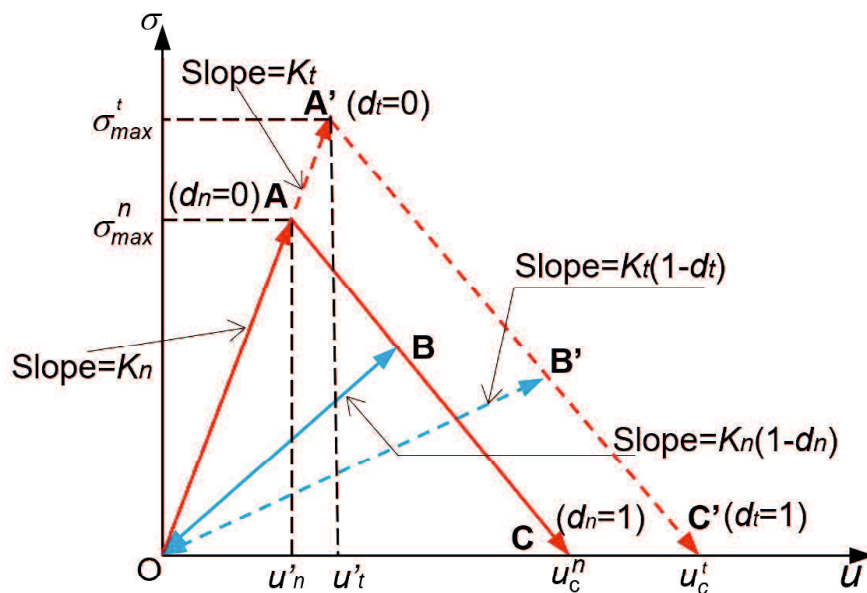
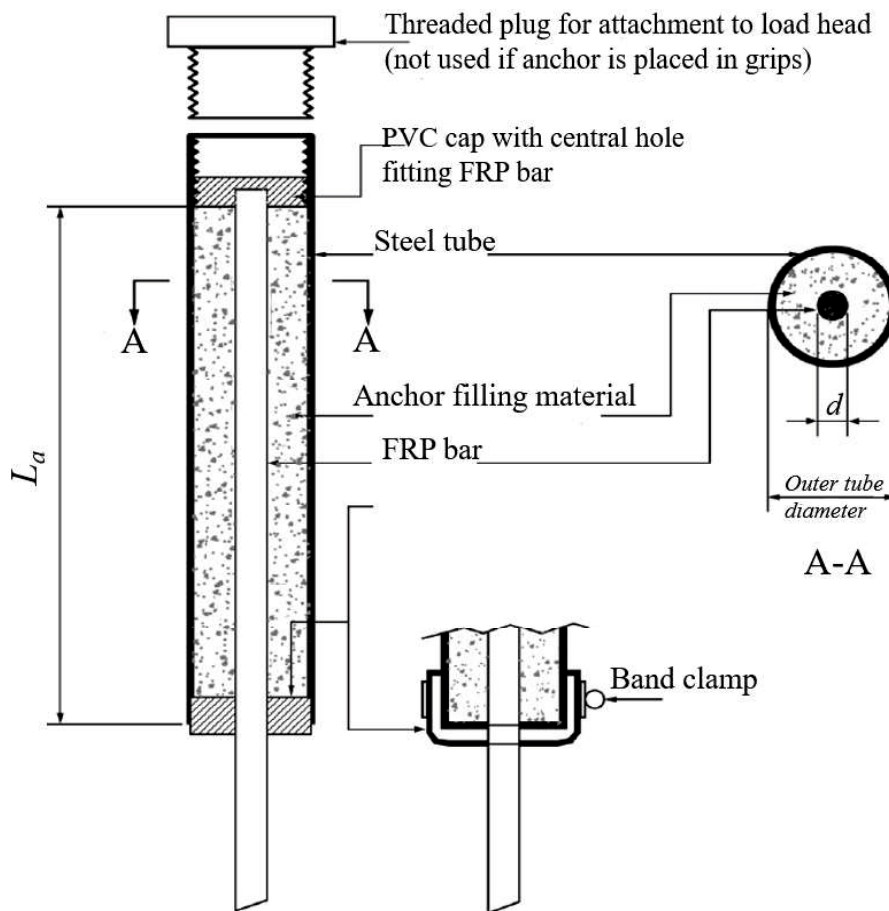


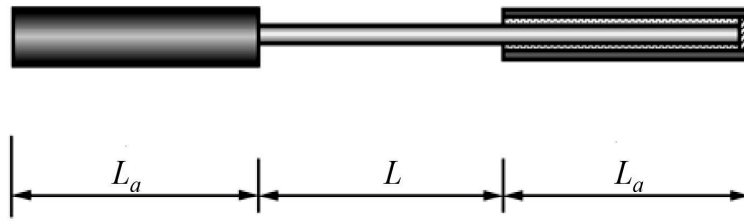
Figure 2.12. Bilinear traction-separation law

## 2.4. Model of FRP rods in bond-type anchorage system

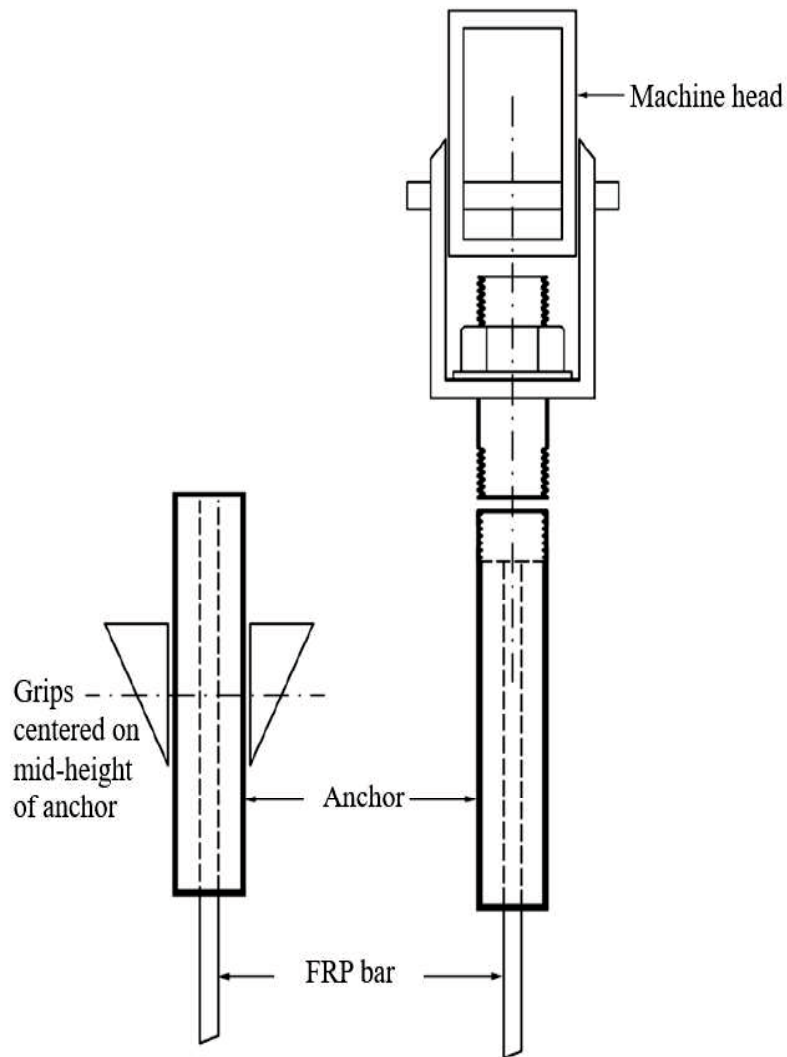
A numerical model was proposed for FRP rods with sizes recommended by standard ASTM D7205/D7205M-06 2016 [72]. Figure 2.13 shows details of a tensile test of an FRP rod. The FRP rod should be aligned axially with the steel tube. The steel tube sizes, including the bond length  $L_a$  and outside diameter, were recommended in the standard [72]. The free length  $L$  in Figure 2.13 (b) should be higher than 380 mm, nor 40 times the effective rod diameter. The minimum thickness of the steel tube and filling material are 4.8 and 4.0 mm, respectively. In addition, the steel tube thickness is enough to maintain tensile stress that is lower than the yielding strength.



(a)



(b)



(c)

Figure 2.13. Testing system in ASTM D7205/D7205M-06 (2016): (a) example anchor details, (b) dimensions of test specimens and steel tubes, (c) example of the attachment of anchor to grips or threaded collets [72].

The tensile model of FRP rods in bond anchorage systems was introduced in previous studies [44]. However, this study concentrated on the behavior of the filling material. CFRP rods are transversely isotropic materials. However, Puigvert *et al.* [44] considered the CFRP rod as isotropic material in the tensile model. This is the main limitation of this study. Moreover, the study models CFRP rods with a coarse mesh. Therefore, a new model should be proposed for investigating the tensile behavior of FRP rods in the bond anchorage systems.

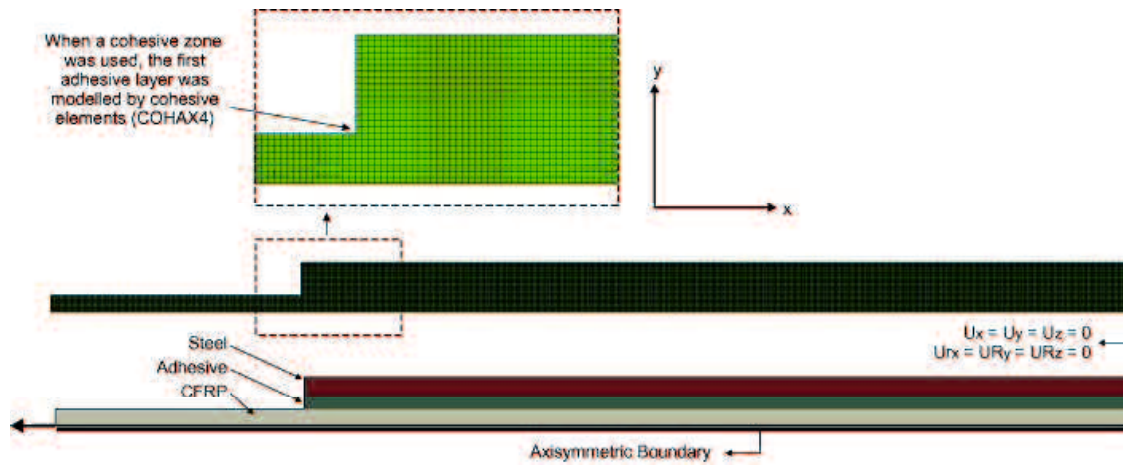


Figure 2.14. Tensile model of CFRP rod in bond anchorage system [44].

Two models were presented with a consideration of the bond interfacial behavior between FRP rods and the filling material and between steel tubes and the filling material. The first model was simulated with a perfect bond at interfaces between materials. The second model considered the partially-bonding strength by using the CZM model. The FRP rod was modeled as transversely isotropic material. The models were used to investigate the tensile failure criteria for FRP rods. The major advantage of the models is that the shear-lag effect and failure of FRP rods under tension. The study also applied the submodeling method to enhance the tensile behavior results of FRP rods.

## 2.5. Submodeling technique

Submodeling is a technique in ANSYS [54] that can be used to reanalyze a region of a FEM model. This technique is also called the cut-boundary displacement method. The submodel is cut from the full model, as shown in Figure 2.15. The boundary

conditions of the submodel are interpolated from the nodal results in the full model. To enhance the accuracy of the results, the submodel employs a finer mesh than the full model.

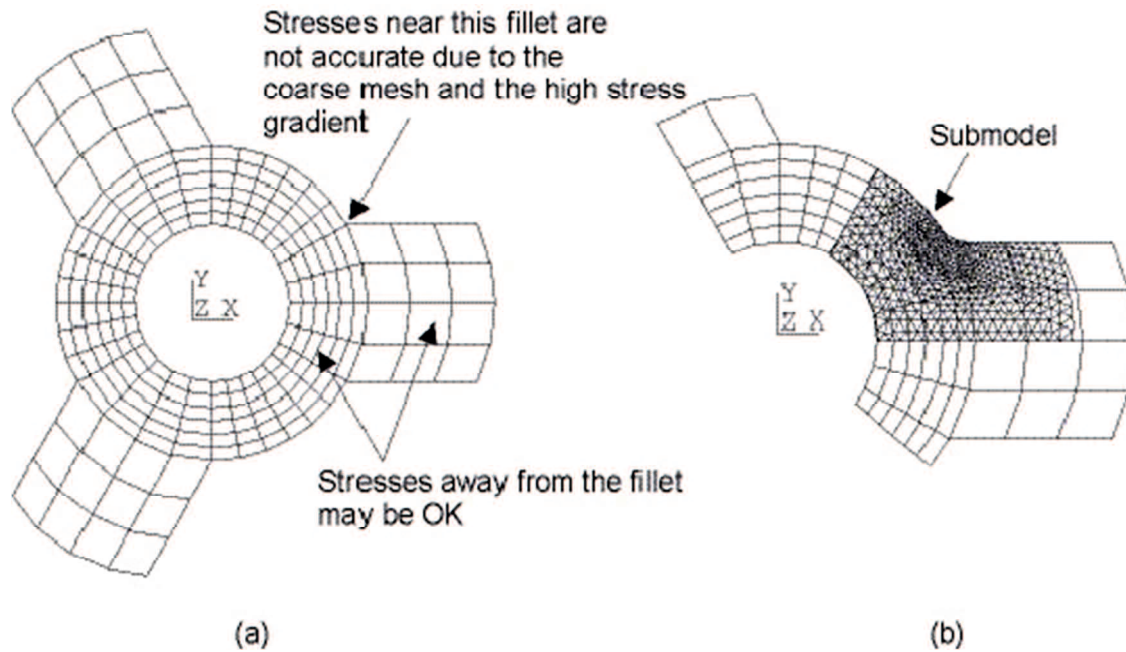


Figure 2.15. Submodeling technique: (a) full model, (b) submodel [54].

## 2.6. Shear-lag effect in FRP rods

The shear-lag effect of composite materials implies the stress transfer between fibers and a matrix, or in the laminate composites. The definition of “shear-lag effect” in this study is only used to analyze the strain/stress distribution of the FRP rods pulled out of filling materials (concrete, mortar, and resin) in NSM systems or bond anchorage systems. Previous studies [37–42] mentioned the shear-lag effect as a reason for reducing the tensile strength of FRP rods. The tensile stress at the outer layer is higher than that at the inner layer. The shear stress along the round surface was transformed to the tensile stress in FRP rods, as shown in Figure 2.16. The shear stiffness plays a key role in the stress/strain transfer between the lateral surface and the core of the rod. FRP rods are transversely isotropic materials, and the in-plane shear stiffness is relatively small. This is the main reason causing the shear-lag effect in FRP rods.

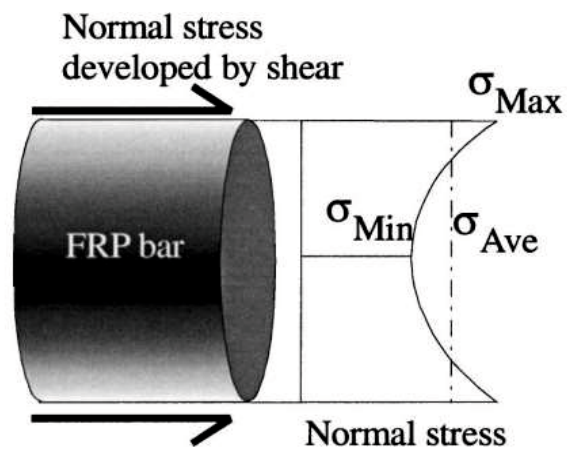


Figure 2.16. Shear-lag effect [42]

## Chapter 3. RVE modeling

### 3.1. Fibers and matrix properties

The present study investigated the tensile properties of Technora FRP rods. Technora is a kind of aramid fiber. The matrix constituting AFRP rods is a vinyl-ester resin. The mechanical properties of Technora fibers and the matrix affect the mechanical properties of FRP rods. Technora is a transversely isotropic material following Equations (1) - (3). Table 1 shows the properties of Technora fibers collected from the previous study [36]. However, the material properties and geometry for the microstructure of Technora fibers are limited. Transverse Young's modulus was collected from a transverse compressive test on Technora fibers [73]. Some material properties such as shear modulus  $G_{12}$ , Poisson's ratios  $\nu_{12}$  and  $\nu_{23}$  were estimated from another aramid fiber showing approximate behavior [74]. The diameter of Technora fibers was chosen as 12  $\mu\text{m}$ . The information of Technora is limited. Therefore, the study investigated Technora in two cases: having enough properties and having only longitudinal modulus.

Table 1. Properties of Technora fibers and a matrix [36].

Materials	Tensile strength (MPa)	Young's modulus (MPa)	Shear modulus (MPa)	Ultimate strain (%)	Fiber ratio (%)	Poisson's ratio
Aramid fibers	3500	$E_1=74000$ $E_2=1590$	$G_{12}=2400$ $G_{23}=641^*$	4.6	65	$\nu_{12}=0.600$ $\nu_{23}=0.240$
Vinyl ester resin	90	3400	-	>4.6	-	0.373

\* The value follows the relationship  $G_{23}=E_2/(1+\nu_{23})$ .

Noritake *et al.* [36] presented the properties of the vinyl ester resin in Table 1. However, this study did not show the tensile stress-strain curve of the vinyl ester resin. The nonlinear stress-strain curve for vinyl ester resin was estimated based on its properties, as shown in Figure 3.1.

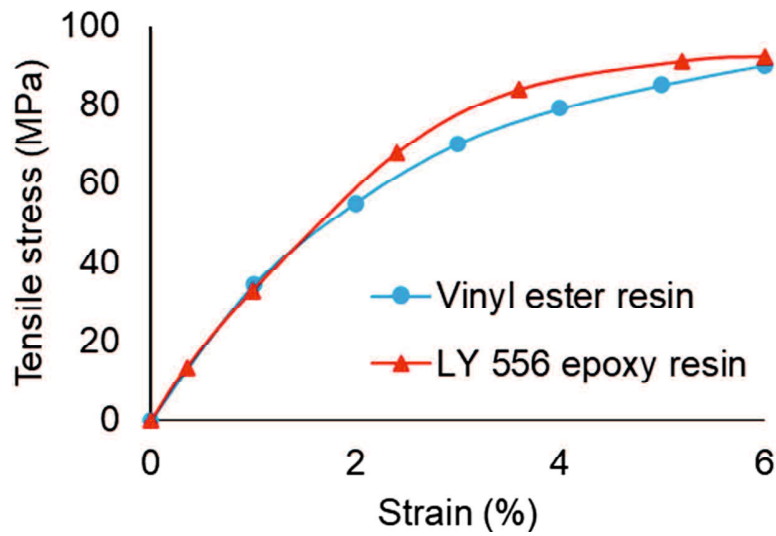


Figure 3.1. Stress-strain curves of resins.

### 3.2. RVE-1

The section below shows the predicted properties of FRP rods by using the RVE-1 model. As shown in Section 2.1, the RVE-1 model has many advantages in predicting engineering constants of UD composites. Both fibers and matrix were assumed as linear materials. The properties of fibers and matrix are shown in Table 1. Technora fiber, a kind of aramid fiber, is a transversely isotropic material. The fiber needs many engineer constants to identify its properties. However, the fiber size is really small to conduct all tests on it. The parameters that could be determined easily are longitudinal modulus  $E_1=74000$  MPa and Poisson's ratio  $\nu_{12}=\nu_{13}=0.6$ . Therefore, to identify the effect of transverse properties of fibers on FRP rods, the present study investigated the properties of Technora fibers in two cases as a transversely isotropic material (A) and isotropic material (B) in Table 2. Moreover, the study built an FRP rod model (C) with isotropic material like a previous study [44]. Model C was employed to assess the appropriateness of the isotropic model.

The volume fraction of fibers is 65%, as reported in Table 1. The fiber diameter is 12  $\mu\text{m}$ . The RVE-1 sizes were chosen as  $a_1=1.766$   $\mu\text{m}$ ,  $a_2=7.065$   $\mu\text{m}$ , and  $a_3=12.235$   $\mu\text{m}$  to adapt this fiber ratio in this study. Fibers and the matrix were simulated using the three-dimension (3D) element named SOLID185 in ANSYS. The model assumed the perfect bond at the

interfaces between the fibers and vinyl ester resin. The calculation followed Equations (12)-(16). The predicted properties of FRP rods were reported in Table 2.

The properties of FRP in case (A) are more accurate than those in case (B). Moreover, the present study compared two cases (A and B) to explain the effect of transverse properties of the fiber on the behavior of FRP rods.

Table 2. Engineering constants of the AFRP materials.

Case	Young's modulus (MPa)	Shear modulus (MPa)	Poisson's ratio
(A) Transversely isotropic fiber	$E_1 = 48806$ $E_2 = 2176$	$G_{12} = 4717$ $G_{23} = 807$	$\nu_{12} = 0.489$ $\nu_{23} = 0.349$
(B) Isotropic fiber	$E_1 = 49547$ $E_2 = 14462$	$G_{12} = 4956$ $G_{23} = 5065$	$\nu_{12} = 0.357$ $\nu_{23} = 0.428$
(C) Isotropic FRP rod	$E_1 = 49547$	$\nu = 0.357$	

### 3.3. RVE-2

As identified in Section 2.2.2, the RVE-2 model with a random distribution of fibers was utilized to predict the strengths of FRP material. All FRP rods have similar mechanical properties. The RVE-2 model results can be applied for all FRP rods. The material properties for fibers were assumed as the linear elastic material whose detail properties were shown in Table 1. Furthermore, the nonlinear stress-strain curve for vinyl ester resin was estimated based on its properties, as shown in Figure 3.1. The sizes of the RVE-2 model were  $a_1=0.25 \mu\text{m}$ ,  $a_2=a_3=13.19 \mu\text{m}$ .

In the RVE-2 model, the CZM model was employed to simulate interfaces between fibers and vinyl ester resin, as shown in Figure 3.2. The interfacial normal strength was determined from the strength ratio  $R_s = \sigma_{max}^n / \sigma_{resin}^y$  is from 10 to 25%. The tensile strength of the vinyl ester resin  $\sigma_{resin}^y = 90 \text{ MPa}$ . The interfacial tangential strength was assumed at 60 MPa, following the previous study [67]. The contact stiffness and interfacial fracture

energy were chosen for both modes I and II of the RVE-2 model as  $10^8$  GPa/m and  $100$  J/m<sup>2</sup> [75], respectively, which were reported in Table 3. The elastic stiffness  $K = 10^8$  GPa/m was large enough to establish displacement continuity at fiber-matrix interfaces and avoid any variation of stress fields around fibers [75]. All parameters of the CZMs were reported in Table 3. Each value of strength ratio  $R_s$  relates to an RVE-2 model. The study employed the SOLID185 element in ANSYS to model fibers and matrix. CONTA173 and TARGE170 elements were applied to simulate the interfaces between the fibers and the vinyl ester resin.

Table 3. CZM parameters for modes I and II in the RVE-2 model simulation.

Strength ratio ( $R$ ) (%)	Tensile strength ( $\sigma_{resin}^y$ ) (MPa)	Interfacial normal strength ( $\sigma_{max}^n$ ) (MPa)	Interfacial tangential strength ( $\sigma_{max}^t$ ) (MPa)	Contact stiffness ( $K_n, K_t$ ) (GPa/m)	Fracture energy ( $G_c^I, G_c^{II}$ ) (J/m <sup>2</sup> )
10	90	9.0	60	$10^8$	100
15	90	13.5	60	$10^8$	100
20	90	18.0	60	$10^8$	100
25	90	22.5	60	$10^8$	100

With a fiber ratio of 65%, the study indicated that the random distribution of fibers did not affect the results. The predicted tensile strengths of the RVE-2 models were summarized in Table 4. Four failure criteria were established from simulation results based on four levels of the estimated interfacial normal strength. The increase of the interfacial normal strength  $\sigma_{max}^n$  from 9.0 to 22.5 MPa in Table 3 induces the rise of the transverse tensile strength ( $F_{2tf}$  or  $F_{3tf}$ ) from 34.2 (FC-1) to 52.3 MPa (FC-4) in Table 4. A similar trend is found in the case of shear strength  $F_{23f}$ . The longitudinal tensile strength  $F_{1tf}$  and shear strength  $F_{12f}$  or  $F_{13f}$  remain unchanged at about 2238 and 160 MPa, respectively. The study found that the longitudinal tensile strength is much higher than the transverse tensile strength. The compressive strength was estimated from the longitudinal tensile strength of the RVE-2 models and the yielding strength of vinyl ester resin. With respect to the tensile strength of FRP rods, it should be noted that the estimated compressive strength does not affect the

failure criteria. The failure criteria in Table 4 will be used to predict the tensile damage of FRP rods.

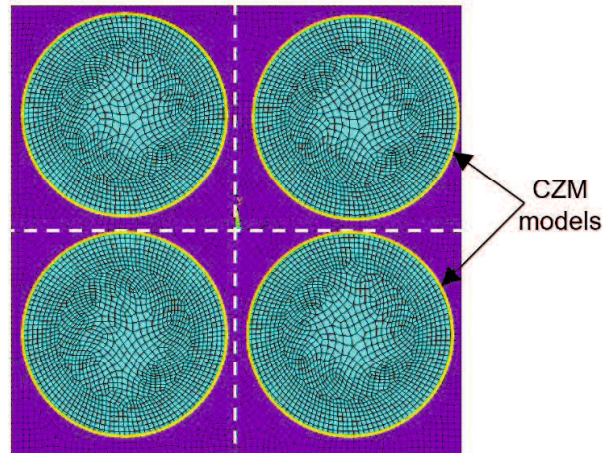


Figure 3.2. CZM models at fiber-matrix interfaces.

Table 4. Failure criteria of AFRP materials.

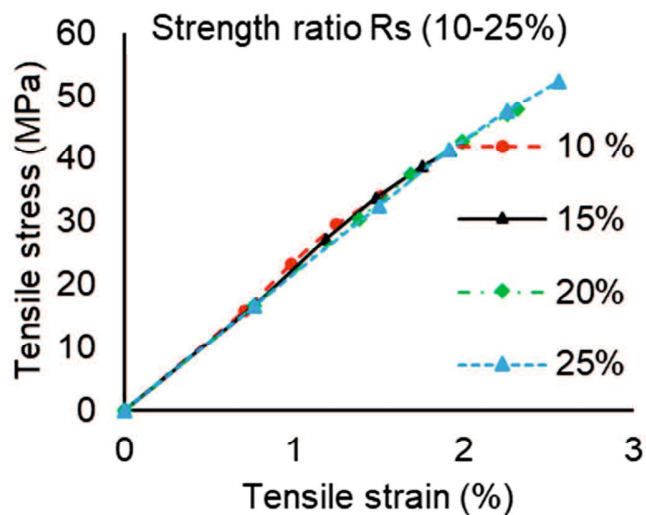
Strength*	Failure criterion			
	FC-1	FC-2	FC-3	FC-4
	(MPa)	(MPa)	(MPa)	(MPa)
(a) Transverse tensile strength ( $F_{2tf}, F_{3tf}$ )	34.2	41.3	47.9	52.3
(b) Transverse compressive strength ( $F_{2cf}, F_{3cf}$ ) <sup>b</sup>	-108.0	-108.0	-108.0	-108.0
(c) Longitudinal tensile strength ( $F_{1tf}$ )	2238.0	2238.0	2238.0	2238.0
(d) Longitudinal compressive strength ( $F_{1cf}$ ) <sup>a</sup>	-1119.0	-1119.0	-1119.0	-1119.0
(e) Shear strength ( $F_{12f}, F_{13f}$ )	159.8	152.9	159.7	159.7
(f) Shear strength ( $F_{23f}$ )	31.9	34.7	36.9	40.7

<sup>a</sup> The estimated values equal half of longitudinal tensile strength.

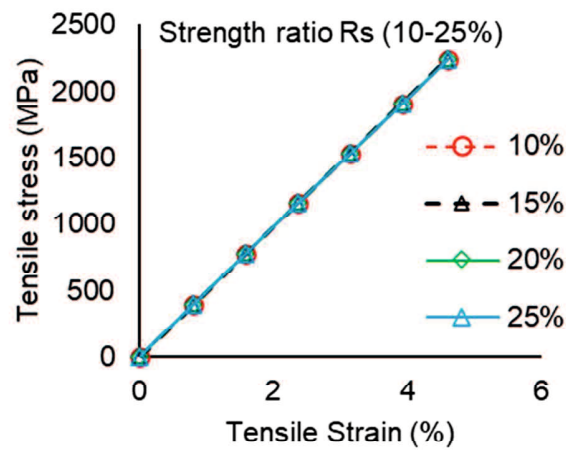
<sup>b</sup> The estimated values equal 120% of the yielding strength of vinyl ester resin.

\* The number 1 denotes the longitudinal direction of fibers; numbers 2 and 3 denote transverse directions of fibers.

The variation of the strength ratio  $R_s$  create various FRP materials with failure criteria. The predicted tensile strengths of FRP materials in longitudinal and transverse directions were reported in Table 4. Furthermore, the mechanical behaviors in three dimensions should be studied to assess the consistent response of the FRP materials in the RVE-2 and global models. Hence, four models with different strength ratios were investigated, and the results were presented in Figure 3.3. The mechanical behavior of the RVE-2 model depends on fiber and matrix properties. However, the fiber ratio is also a significant factor that can control RVE behavior (following fiber or matrix properties). With a 65% fiber ratio, the stress-strain relationship is assumed as linear in the longitudinal and transverse directions of the RVE-2 model, as shown in Figure 3.3.



(a) Transverse direction



(b) Longitudinal direction

Figure 3.3. Tensile stress-strain curve of the RVE-2 models.

Figure 3.3 confirms that the FRP material response of the RVE-2 models is consistent with the transversely isotropic properties of FRP rods in tensile models. Hence, the failure criteria established from the predicted strengths could be applied to validate the damage of FRP rods in tensile models.

## Chapter 4. Numerical modeling of tensile tests

### 4.1. Materials

The mechanical properties of the simulated FRP rod material were reported in Table 2. The filling material was chosen with high strength and strain to transfer the tensile force from the machine to the AFRP rod. Standard ASTM D7205/D7205M-06 2016 [72] indicated that the transverse modulus of AFRP rods is lower than other FRP materials (GFRP, CFRP). As shown in Table 2, the present study confirmed a low transverse modulus of AFRP rods (2176 MPa). The low transverse modulus of AFRP rods could lead to difficulty in gripping the rods to anchors by the cementitious grout [72]. The pull-out phenomenon was confirmed in tensile tests on AFRP rods in grouted anchorages [76–78]. Therefore, the recommended filling material is a polymer resin in such cases, as recommended in the standard [72]. Moreover, the ultimate longitudinal strain of FRP rods was prescribed as the ultimate strain of Technora fibers (4.6%), as shown in Table 1. As a result, Technora rods showed a large longitudinal tensile deformation.

The chosen filling material had high tensile strength, bond strength, and large strain deformation to transfer the tensile force from the machine to the AFRP rod. The present study utilized Araldite epoxy resin (LY 556) which combined with hardener HY 917 and accelerator DY 070 as a filling material [79]. The properties of epoxy LY 556 were shown in a previous study [79]. Figure 3.1 shows the stress-strain curve in the tension of LY 556 at room temperature (22 °C) [79].

The steel tube must have enough thickness to guarantee that the failure will occur in the FRP rod. Hence, the tube sizes varied to adapt with various FRP rod diameters. The steel tube was used for transferring the tensile force from the applied load to the FRP rod. This study employed the NPS 1<sup>1/4</sup> - Schedule 80S tube from MBM tubes [80]. The tube characteristics follow American National Standard (ANSI B36.19 Stainless Steel Pipes), ASTM A 312/A 312M-01a. The steel tube sizes were recommended in the standard [72]. The properties of steel tubes and filling material were reported in Table 5.

Table 5. Epoxy and steel tube properties in the analysis models.

Material	Young's modulus (MPa)	Tensile strength (MPa)	Poisson's ratio
Epoxy LY 556 [79]	3800	92.2	0.37
Steel tube grade 310S1 1/4 schedule 80S [80]	200000	205.0* 515.0	0.30

\* Yield strength

#### 4.2. Numerical models with perfect bond

The model of FRP rods in tensile tests with full-bonding behavior was applied in two cases of FRP material in Table 2. Vo and Yoshitake [45] modeled FRP rods with FRP material (A). The numerical analysis model of a tensile test followed the standard ASTM D7205/D7205M-06 (2016) [72]. The sizes of the model are shown in Table 6.

Table 6. Sizes of the analysis model [45].

Diameter of FRP bar (mm)	Outside diameter of the steel tube (mm)	Anchor length ( $L_a$ ) (mm)	Free length ( $L$ ) (mm)	Thickness of epoxy resin (mm)	Thickness of steel tubes (mm)
3				26.5	
4	42.2	300	380	24.5	4.85
6				20.5	
8				16.5	

However, the simulation of a full model costs much computation. The analysis model is symmetric in tension. As shown in Figure 4.1 (a), using a half model can reduce a large

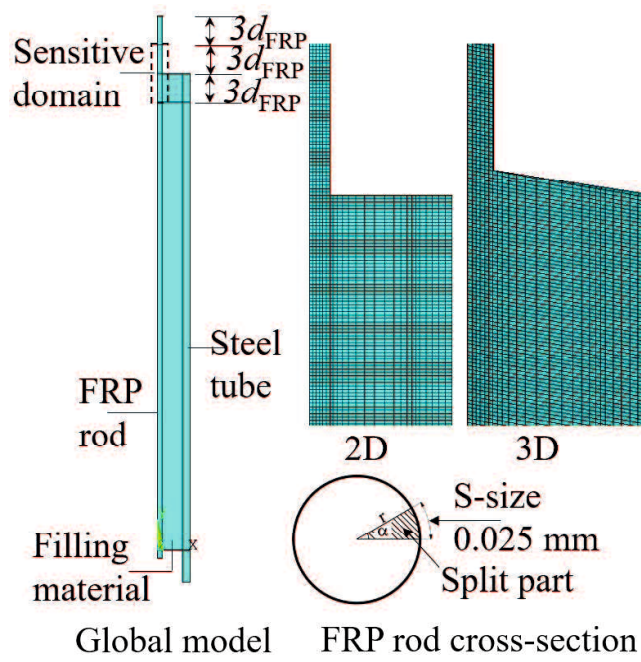
number of elements. The half model still costs much computing time. The half model uses the y-axis as the axis of rotational symmetry. In addition, the tensile load is also symmetrical. To optimize the computation, this study proposed a divided model based on the axisymmetric modeling method in ANSYS, as shown in Figure 4.1 (b). The divided model was split from the half model in Figure 4.1 (a) with an angle  $\alpha$ . The value of  $\alpha$  was calculated from the FRP rod radius and the element size 0.025 mm in Figure 4.1 (b). The divided model was called the global model adapting all details of the testing system.

The present study indicated that the shear lag only affects the domain (six times  $d_{FRP}$  of the free length and three times  $d_{FRP}$  of the bond length), as shown in Figure 4.1 (b). This finding helped to reduce the free length in the global model. Figure 4.2 presents the boundary conditions of the global model. The applied displacement on the steel tube in y-direction causes strains and stresses in the filling material and the FRP rod. The study defined an unbonded domain (5 mm) to avoid the large deformation of the vinylester resin at the interface between the FRP rod and filling material.

The stress distribution around the anchorage was complicated. Hence, a technique called the sub-modeling in ANSYS was employed for obtaining more accurate results in the sensitive domain in Figure 4.1 and Figure 4.2. The sub-model only simulated the FRP rod in the sensitive domain (with a finer mesh) sized in the length of six times the rod diameter in Figure 4.2. The sub-model boundary conditions were interpolated from the global model results in Figure 4.1 (b). The global model and sub-model used a 3D-eight node solid element named SOLID185 in ANSYS [54]. The simulation assumed the full-bonding and continuity among materials.



(a)



(b)

Figure 4.1. Analysis model in ANSYS: (a) half model; (b) divided model (global model).

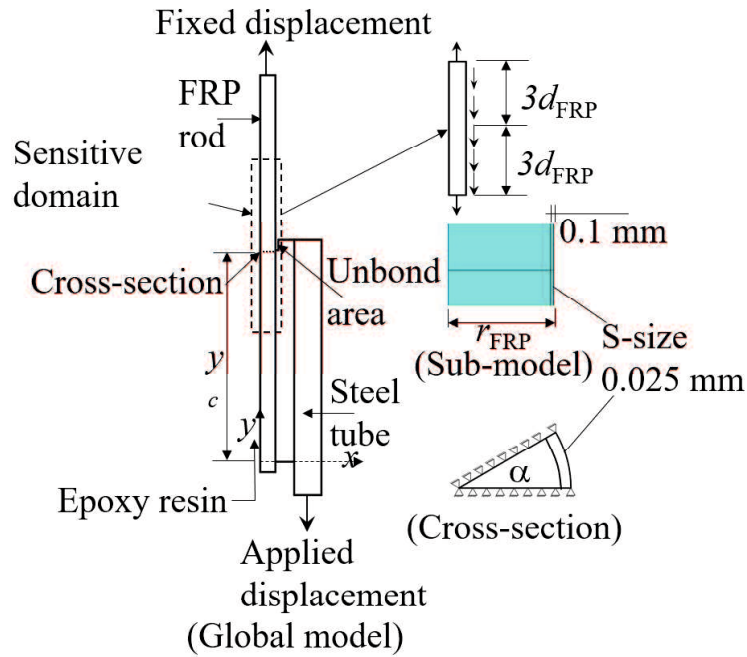


Figure 4.2. Boundary conditions of the analysis models.

It is well known that simulation results are often affected by the element size. Vo and Yoshitake [45] varied element sizes in the global model and sub-model of the material (B) model. Table 7 summarizes all element sizes in the global model and sub-model. The global model was meshed with G-size at the sensitive domain and larger sizes at the others. The sub-model used a more refined mesh with S-size to enhance accuracy. The S-size=0.025 mm denoted the unchanged element size in the region of 0.1 mm close to the lateral surface of the FRP rod in the sub-model, as shown in Figure 4.2. The study employed three kinds of G-size (0.2, 0.25, and 0.5 mm) in the global model and three kinds of S-size (0.05 and 0.1 mm at inner domain, and an unchanged value of 0.025 mm at outer domain) in the sub-model. Six simulations were conducted on the FRP rod ( $d=6$  mm) to find the convergence value of ultimate tensile forces.

Table 7. Element sizes and ultimate tensile force results of model (A).

D (mm)	G-size* (mm)	S-size* (mm)	Ultimate tensile force (kN)
6	0.50	0.10 & 0.025	54.81
	0.50	0.05 & 0.025	52.84
	0.25	0.10 & 0.025	52.55
	0.25	0.05 & 0.025	52.55
	0.20	0.10 & 0.025	51.97
	0.20	0.05 & 0.025	51.97

\* G and S denote the global model and sub-model, respectively

The sub-model was considered as layers of elements following the radius direction. The averaging theory in Equation (25) was proposed to find the average axial tensile stress in the y-axis in the cross-section. Table 8 shows an example for determining average tensile stress by using Equation (25).

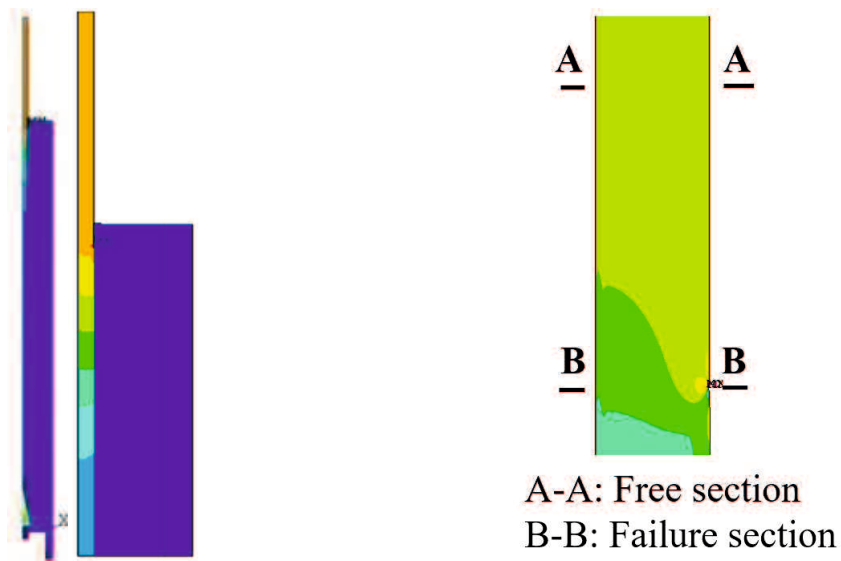
$$\bar{\sigma}_j^y = \frac{1}{V} \int_V \sigma_i^y(x, y, z) dV = \frac{\sum_i \sigma_i^y V_i}{V_j} \quad (25)$$

where  $\sigma_i^y$  is the axial tensile stress element  $i_{th}$  in layer  $j_{th}$ ;  $\bar{\sigma}_j^y$  is the average axial tensile stress of layer  $j_{th}$ . For example, Figure 4.3 (c) presents a cross-section of the FRP rod ( $d=6$  mm) containing 33 layers of elements along the radius.

Table 8. Tensile stress of each layer in the failure section in the model (A)-D6

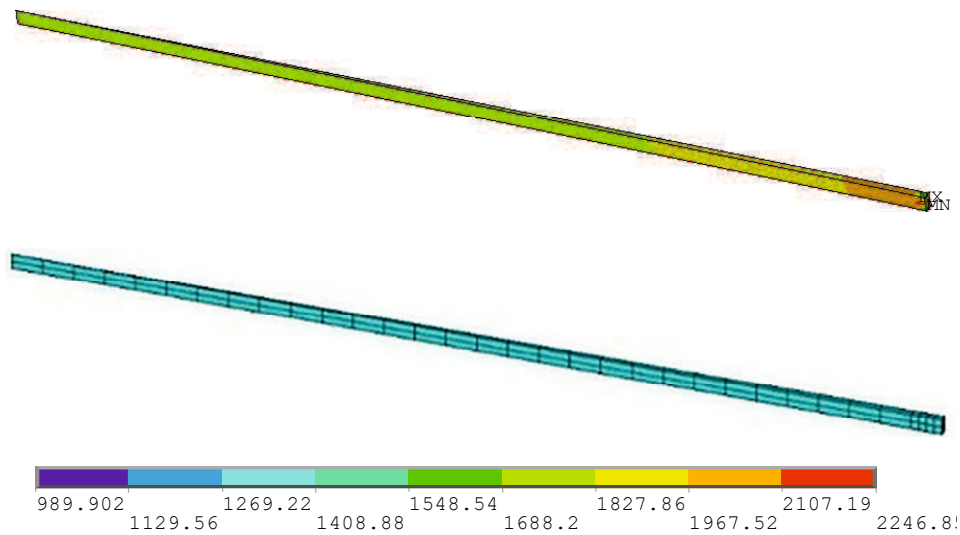
Layer $j^{th}$	$V_j$	$\sum_i \sigma_i^y V_i$	$\bar{\sigma}_y^j$
	(mm <sup>3</sup> )	(MPa.mm <sup>3</sup> )	(MPa)
1	0.000001	0.00183	1746.87
2	0.000003	0.00553	1751.88
3	0.000005	0.00923	1754.13
4	0.000007	0.01292	1755.00
5	0.000009	0.01662	1755.99
6	0.000012	0.02033	1757.21
7	0.000014	0.02405	1758.71
8	0.000016	0.02777	1760.49
9	0.000018	0.03151	1762.57
10	0.000020	0.03526	1764.97
11	0.000022	0.03903	1767.71
12	0.000024	0.04281	1770.83
13	0.000026	0.04662	1774.36
14	0.000028	0.05045	1778.35
15	0.000030	0.05431	1782.84
16	0.000033	0.05821	1787.91
17	0.000035	0.06214	1793.64
18	0.000037	0.06612	1800.14
19	0.000039	0.07016	1807.53
20	0.000041	0.07425	1816.01
21	0.000043	0.07843	1825.80
22	0.000045	0.08269	1837.21

Layer $j^{th}$	$V_j$	$\sum_i \sigma_i^y V_i$	$\bar{\sigma}_y^j$
	(mm <sup>3</sup> )	(MPa.mm <sup>3</sup> )	(MPa)
23	0.000047	0.08707	1850.70
24	0.000049	0.09158	1866.83
25	0.000051	0.09628	1886.56
26	0.000053	0.10118	1911.06
27	0.000055	0.10636	1942.50
28	0.000056	0.11180	1983.74
29	0.000057	0.11666	2031.04
30	0.000014	0.02958	2055.74
31	0.000014	0.02969	2073.41
32	0.000014	0.02908	2055.36
33	0.000014	0.02707	1966.70



(a)

(b)



(c)

Figure 4.3. Tensile stress in the y-direction of the FRP rod( $d=6$  mm): (a) around anchorage of the global model, (b) around the failure section of the sub-model, and (c) in the failure section of the sub-model.

The maximum applied displacement was determined at the value enforcing the ultimate stress  $\sigma_y$ , approximately 2238 MPa. The ultimate tensile force of the FRP rod was determined when the FRP rod was broken at the failure section. At this time, the tensile stress in the free

section in Figure 4.3 was the same from the core to the lateral surface of the FRP rod. The tensile stress was called the tensile strength of the FRP rod in such a case. The ultimate tensile force of the FRP rod was determined as follows

$$P_u = \sigma_u^{rod} A \quad (26)$$

where  $P_u$  is the ultimate tensile force of the FRP rod.  $A$  and  $\sigma_u^{rod}$  are the area of the cross-section and the tensile strength of the FRP rod, respectively.

In the full-bonding model, the interfacial bond induces high transverse tensile stress in the FRP rod elements. The FRP elements can be broken by transverse tension before longitudinal tension. Therefore, the present study only applied the longitudinal strength as the failure criterion in the full-bonding models.

#### **4.2.1. Model A results**

Table 7 and Figure 4.4 present the effect of the element sizes on the ultimate tensile force. Six cases of various element sizes were applied to find the ultimate tensile forces. The tensile force value converges at the G-size from 0.2 to 0.25 mm. and S-size from 0.05 to 0.1 mm in Figure 4.4. The element size affects the number of elements and computing time. Hence, the appropriate G-size and S-size are 0.25 and 0.1 mm, respectively. Four types of diameters were simulated with these element sizes. The S-size (0.025 mm) remains unchanged at the area close to the lateral surface of the FRP rod in all cases.

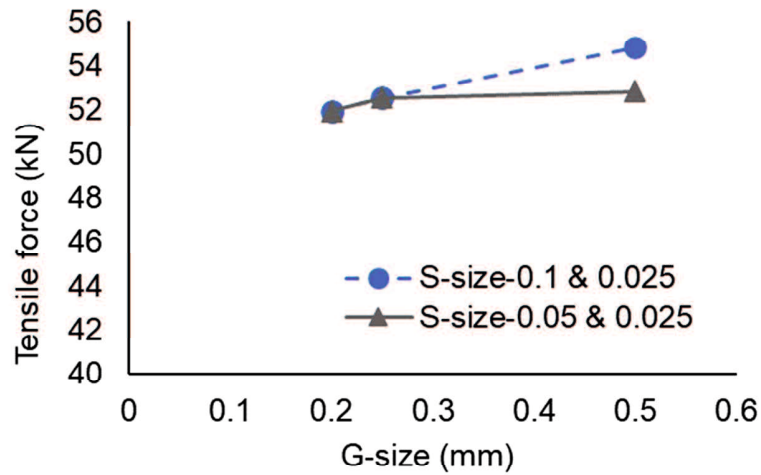


Figure 4.4. Tensile forces versus element sizes of the FRP rod ( $d=6$  mm).

The shear-lag effect was reported in Figures 4.3, 4.5, and 4.6. Figure 4.3 shows the axial tensile stress distribution in the global model of FRP rod ( $d=6$  mm) under a displacement  $u_y = 2.675$  mm on the steel tube head. Figure 4.5 shows the tensile stress  $\sigma_y$  in three sections. In the failure section, the tensile stress is higher in the outer layers and lower in the inner ones. The stress distribution of the failure section in Figure 4.5 is similar to that in Figure 2.16. The failure section and free section positions are at  $y_c=295$  mm and  $y_c=318$  mm, respectively. The cross-section ( $y_c=296$  mm) is the intermediate phase between the two above sections. The shear-lag only affected the domain from  $y_c=295$  to 297 mm. The failure element contains the nodal stress of 2238 MPa. However, the stress of the failure element interpolated from the integration point results was lower, approximately 2073 MPa. The tensile stress in the failure section decreases from a maximum (approximately 2073 MPa in the outer elements) to a minimum (approximately 1747 MPa at the core), reduced by 16%. The tensile stress in the free section remains at an approximate value of 1858 MPa, reaching 82.8% of the tensile strength of the FRP material 2238 MPa. The tensile stress in the free section denotes the FRP rod tensile strength  $\sigma_u^{rod}$  in Equation (26). Hence, the tensile strength of the FRP rod is lower than that of the FRP material.

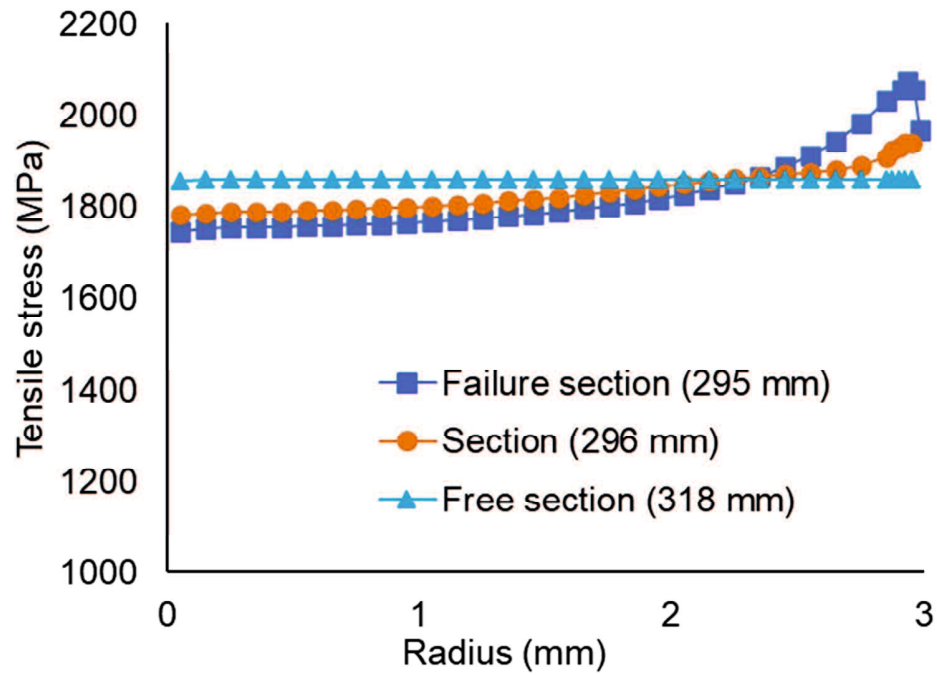
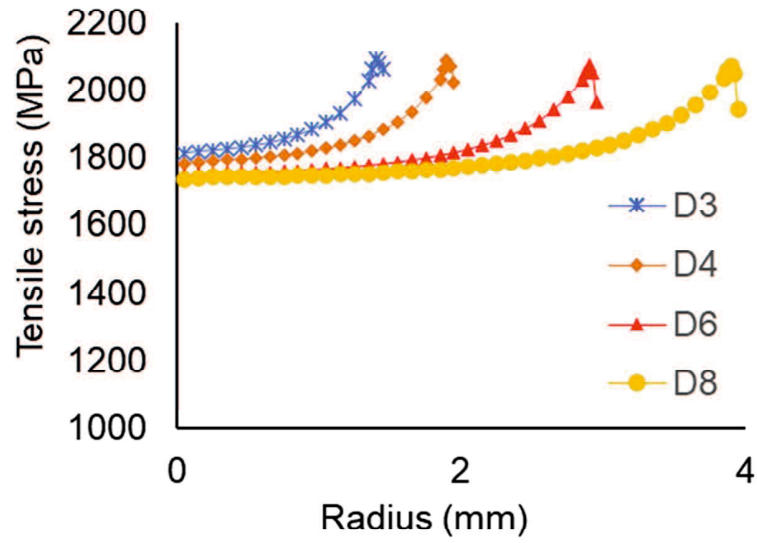
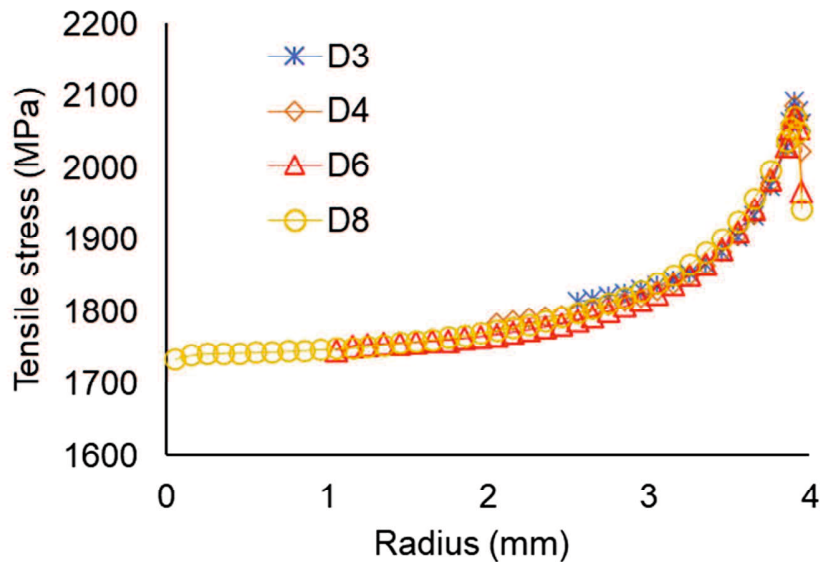


Figure 4.5. Axial tensile stress distribution in cross-sections of the FRP rod ( $d=6$  mm).

The theoretical ultimate tensile force of the FRP rod ( $d=6$  mm) could reach the value of 63.44 kN, with a material tensile strength of 2238 MPa. The ultimate tensile force (52.55 kN) simulated in the present study was lower than that of the theory, just reaching 82.8%. However, the simulation result approximates the experimental value (53.13 kN) [36], with a deviation of 1.1 %. In addition, Noritake *et al.* [36] measured the axial tensile strain in the free length of the FRP rod ( $d=6$  mm), around 3.7%. It is consistent with the simulated free-length strain of 3.8%, with a deviation of 2.7%. The maximum strain in the free length is lower than that of the FRP material (4.6%). This finding indicates that the failure section is out of the free length and close to the anchorage. These results confirm the accuracy of the present model. This phenomenon is similar to tensile testing results in previous studies [76,81–84]. In addition, Figure 4.6 shows the existence of the shear-lag effect in the failure sections of various diameters. The results demonstrated a nonlinear relationship between the radius and the axial tensile stress.



(a)



(b)

Figure 4.6. Distribution of axial tensile stress on the failure sections: (a) separated curves of diameters; (b) combined presentation based on the D8 curve.

The shear-lag effect is one of the main reasons affecting the axial tensile stress distribution in the failure section of the FRP rod. It hardly impacts on the free length. The failure section is much more damaged than the free section. The present findings indicate

that the FRP rod rupture must appear at the failure section. The shear-lag effect reduces the ultimate tensile capacity of FRP rods.

The stress distribution on the failure section is a function of the radius. Figure 4.6 (a) shows the separated curves of various FRP rods. The maximum stress at the outer elements of all diameters is similar to each other, approximately 2073 MPa. The study presented all curves on the D8 coordinate system to assess the shear-lag effect between diameters, as shown in Figure 4.6 (b). The findings show a similar rule of the stress decrease along the radius of four types of diameters. Two phases characterize the relationship at the failure section; namely, the axial tensile stress significantly decreases in the outer domain limited to 1 mm from the lateral surface of all diameters and then slightly goes down in the other domain. However, four outermost layers close to the lateral surface of the FRP rod show a dramatic fluctuation of the stress variation. The reason for this phenomenon is the significant effect of the shear-lag in this domain.

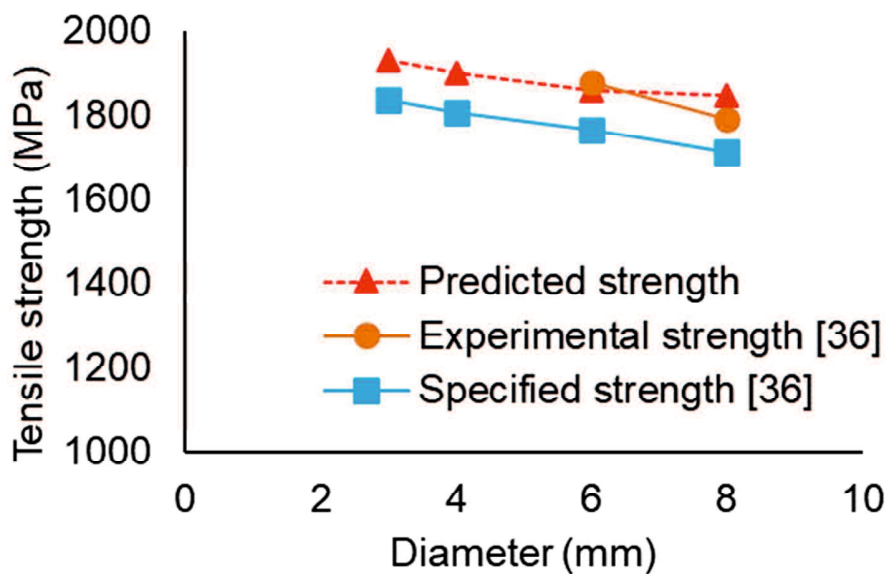


Figure 4.7. Tensile strength decrease versus diameter.

Figure 4.7 shows the decrease of tensile strengths of four diameters from D3 to D8, with 6.8% for specified strength and 4.4% for predicted strength. The predicted strength follows the rule of the experimental and specified results of the previous study [36]. As considered in Figure 4.6, the failure of FRP rods appears at the lateral surface containing

higher stress. All FRP rods made of a similar volume fraction have a similar material tensile strength. FRP rods are ruptured when their tensile stress at the lateral surface reaches the material tensile strength. However, the diameter increase induces a decrease of tensile stress at the core of the FRP rod, as shown in Figure 4.6 (b). Consequently, the FRP rod is ruptured when tensile stress at the core is lower than that at the lateral surface. The present findings demonstrate that the diameter is one of the main factors affecting the tensile strength of the FRP rods.

The study had shown a procedure to predict the ultimate tensile forces of the FRP rods ( $d=3, 4, 6, 8$  mm). Table 7 shows the comparison of the specified, experimental, and predicted results. The deviation between the specified and predicted ultimate tensile forces varies from 5.1 to 7.7%. However, the specified values are always lower than the experimental ones because of the safety-factor consideration. Instead, the experimental results are more appropriate for the comparison. The predicted ultimate forces approximate experimental ones, with a deviation from 1.1 to 3.1%. The present results were consistent with previous findings of Noritake *et al.* [36]. These findings confirmed the effectiveness of the proposed model in predicting the ultimate tensile forces of the FRP rods. However, the limitation of the study is that the experimental results of FRP rods ( $d = 3$  and  $4$  mm) in Table 7 were unavailable to compare with simulation ones.

Table 9. Comparison of specified, experimental, and predicted results

Diameter (mm)	Ultimate tensile force $P_u$ (kN)			Deviation (%)	
	Specified <sup>a</sup>	Experimental <sup>a</sup>	Predicted <sup>b</sup>	Spe-Pre <sup>*</sup>	Exp-Pre <sup>*</sup>
3	13.00	N/A	13.66	5.1	N/A
4	22.70	N/A	23.86	5.1	N/A
6	49.90	53.13	52.55	5.3	1.1
8	86.10	90.00	92.77	7.7	3.1

<sup>a</sup> The results in the previous study [36].

<sup>b</sup> The results in the present study.

<sup>\*</sup> Pre: predicted; Spe: specified; Exp: experimental.

The present findings indicate the existence of the shear-lag effect and the failure section in the FRP rod by mechanical and numerical theory. It also clearly demonstrates the shear-lag phenomenon referenced in Firas *et al.* [43] and Achillides *et al.* [42]. The failure section is much more damaged than other cross-sections, and the FRP rod must be ruptured at this section. The shear-lag effect only causes the nonlinear distribution of the axial tensile stress in the cross-sections close to the anchorage. The stress profiles in the failure sections of all diameters include two phases: significantly decreasing in outermost layers and slightly declining in the other layers. The present study confirmed that the increase of the diameter induces the decrease of the tensile strength. The proposed model is applicable in predicting the ultimate tensile capacity of any pultruded FRP rod. The deviations between the simulation and experimental results are unremarkable.

#### **4.2.2. Model B results**

The properties of FRP material in model B were predicted by Vo and Yoshitake [85]. However, the tensile model in the previous study [85] employed coarse meshes, with G-size=0.5 mm and S-size=0.25 mm. As a result, the accuracy of the results is low. Therefore, the present study rebuilt the model with the same sizes of elements in model A. Model B was simulated to compare the effects of fiber properties in FRP rods. Therefore, the study only conducted a simulation of FRP rod D6 in such a case. The results of longitudinal tensile stress were shown in Figure 4.8. The tensile stress in model B shows a similar trend to that in model A. The tensile stress in the failure section significantly decreases from the lateral surface to the core of FRP rod D6. The deviation between the maximum and minimum tensile stresses is around 20%.

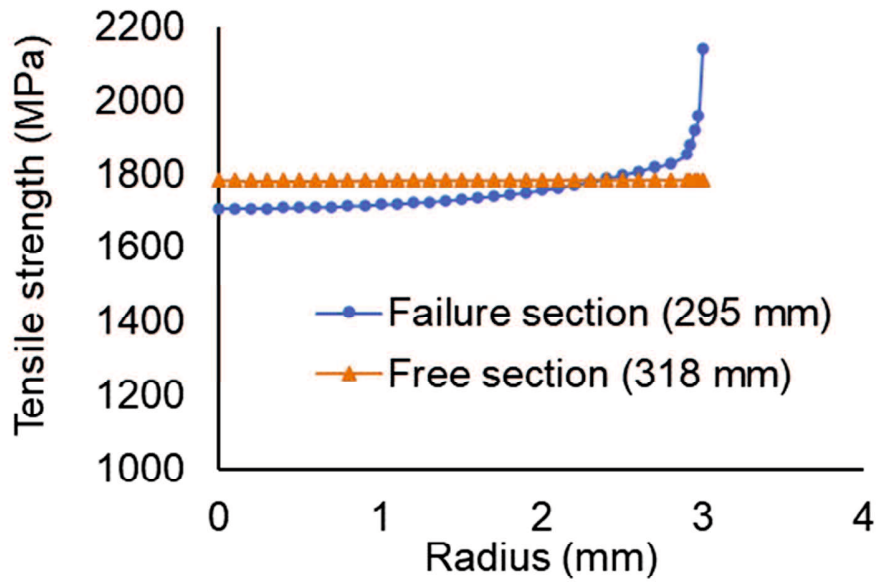


Figure 4.8. Axial tensile stress distribution in cross-sections of the FRP rod ( $d=6$  mm) - model B.

#### 4.2.3. Model C results

Model C is based on the idea of the isotropic CFRP rod model in a previous study [44]. The study built a numerical model AFRP with the same diameter as mode B. The tensile stress distribution in the failure section and free section was shown in Figure 4.9. The stress significantly decreases at the region near the lateral surface of FRP rods. The inner layers show a slight reduction of the tensile stress. The deviation between the maximum and minimum values is approximately 13%.

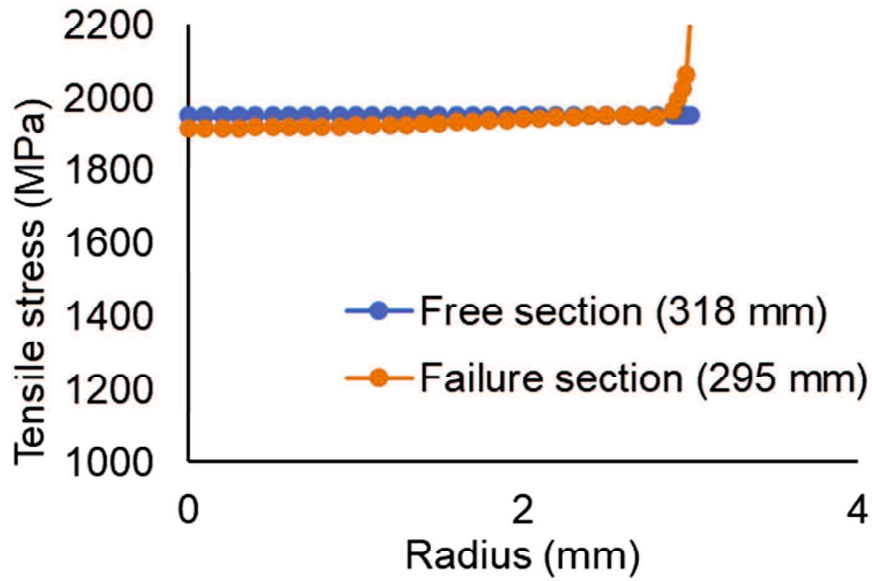


Figure 4.9. Axial tensile stress distribution in cross-sections of the FRP rod ( $d=6$  mm) - model C.

#### 4.3. Numerical models with partially-bonding strength

The model with partially-bonding strength is similar to models A and B. However, the bond length was estimated as 30 times rod diameter  $d_{FRP}$ . Furthermore, the present study indicated that the stresses at any cross-section in the middle area of the free length were equal. Therefore, the free length was reduced in the FE model in such a case. The study employed a free length that equals five times rod diameter.

Due to the axisymmetric property, the study proposed a divided model with an angle  $\alpha$ , as shown in Figure 4.10. The value  $\alpha$  depended on the element  $S_{size-1}=0.125$  mm on the perimeter and the radius of an FRP rod. This FE model was called as the global model, with a mesh size  $S_{size-1}=0.125$  mm on the FRP rod perimeter and  $G_{size}=0.5$  mm in other areas. Consequently, the proposed model could significantly reduce the calculation time comparing to the full model. All materials in the global model were modeled with the element SOLID185 provided by ANSYS. The steel tube and filling material were specified as isotropic materials reported in Table 5. The FRP rod was assumed as the transversely isotropic material due to mechanical properties in Table 2.

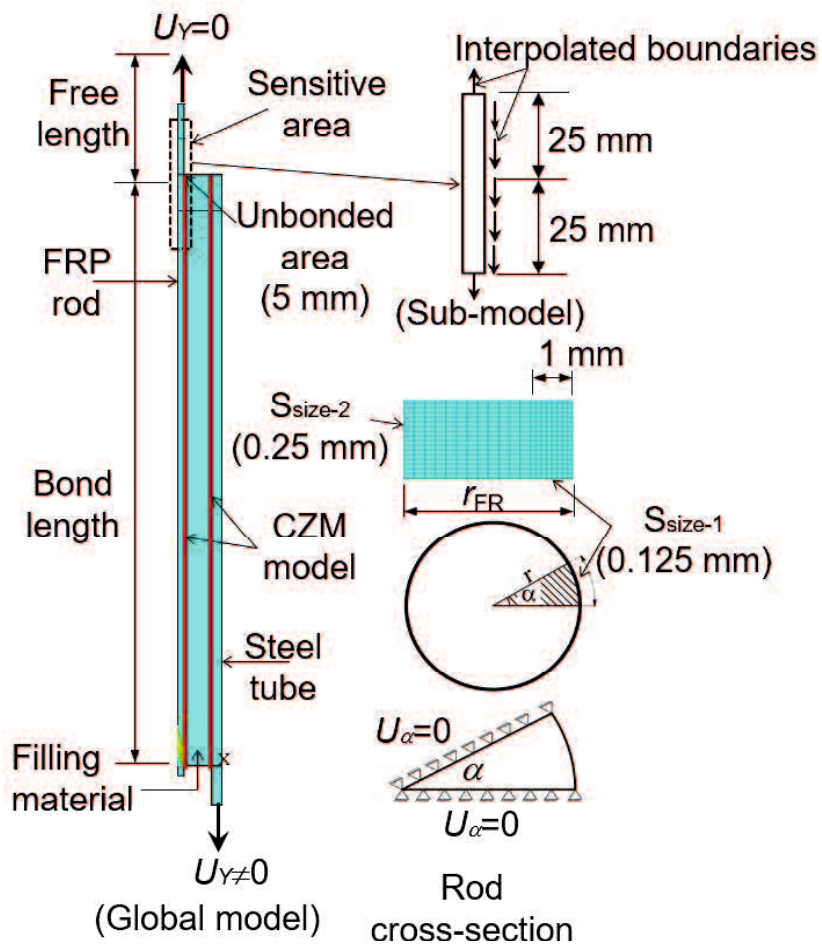


Figure 4.10. Numerical model of FRP rods with partially-bonding strength.

The boundary conditions of the global model were shown in Figure 4.10. The displacement in the y-axis  $U_y \neq 0$  was applied at the head of the steel tube to induce tensile stress in the FRP rod. The FRP rod was fixed  $U_y$  at the free length. In the rotation of angle  $\alpha$ , the displacement  $U_\alpha$  was fixed at both edges. An unbonded area (5 mm) was defined to avoid the concentrated stresses. In addition, the interfaces between the FRP rod and filling material or filling material and the steel tube were simulated as bilinear CZMs, as presented in section 2.3.

In fact, predicting the CZM parameters is a challenge. Indeed, the behavior between two surfaces depends on many effects such as the bond strength of the adhesive, the strengths of adherends, and the quality of contact surfaces. In the global model, the FRP rod is pulled

out of the steel tube. The behavior of the system depends on the shear bonding between the FRP rod and the filling material. Therefore the present study only figured out CZM parameters for mode II. Kessler and Bledzki [86] conducted single-fiber push-out tests using epoxy LY 556-HY 917-DY 070 to find the maximum tangential stress. They showed that the maximum tangential stress  $\sigma_{max}^t$  was higher than 60 MPa. The interface strength depends on the fiber materials. Yademellat *et al.* [67] demonstrated that maximum tangential stress of epoxy LY 556 equaled 60 MPa. Hence, to quantify the bond effect in detail, the present study proposed two values of the maximum tangential stress 60 and 70 MPa.

The contact stiffness remained at a value  $10^6$  GPa/m. Moreover, the maximum tangential separation  $u_c^t$  was varied by changing the displacement ratio  $R_d$  (1, 2, 4, 6, 8), as shown in Equation (27). The change of  $R_d$  denotes the variation of fracture energy release rate  $G_c$ .

$$u_c^t = R_d G_{size} \quad (27)$$

where  $G_{size}=0.5$  mm is the mesh size in the global model.

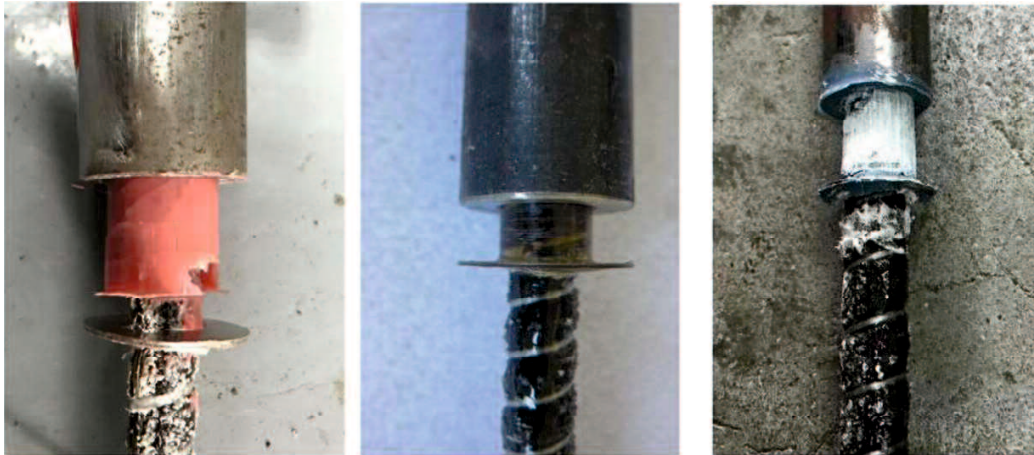
To enhance the accuracy, the submodeling method was applied to model the sensitive area in the FRP rods. The sub-model reanalyzed FRP rods with finer meshes ( $S_{size-1}$  and  $S_{size-2}$ ), as shown in Figure 4.10. After the global model results had been obtained, the code was utilized to find out the failure section. A sub-model was built based on an area of 50 mm around this section. Moreover, the boundary conditions of the sub-model were interpolated from the global model results.

#### 4.3.1. Failure modes of FRP rods

The bond strength in the model was partially limited. Therefore, the failure criteria were applied to predict damages in FRP rods under tensile forces. The global model was applied to simulate the AFRP rods in a previous study [36], then the sub-model was employed to enhance the accuracy of the results in this study. Four numerical models with the same material properties but different diameters (3, 4, 6, and 8 mm) were simulated. Four failure criteria in Table 4 were employed to predict the damage and load-capacity. Finally, all results were summarized in Table 10 (a-d).



(a) Technora AFRP rod [78]



(b) BFRP rods [87]

Figure 4.11. Typical pull-out failure of FRP rods.

The failure of the tensile model could occur at the rod-filling-material interface in Figure 4.11 (a) or steel-tube-filling-material interface in Figure 4.11 (b). The FRP rods were pulled out of the anchors as the bond failed. However, FRP rods were not ruptured in such cases. In addition, the other failure of the tensile model comes from the FRP rods. Figure 4.12 (a) shows the failure of GFRP rods at sections close to the anchors. The FRP rod failure occurs in both longitudinal and transverse directions. In the longitudinal direction, the failure is specified by the fiber tensile strength, called mode (c). By contrast, the delamination is specified by the matrix strength in the transverse direction, called mode (a). A similar

phenomenon is shown in Figure 4.12 (b) and Figure 4.13. The FRP rods rupture in the broom failure mode at the final phase. Figures Figure 4.12 and Figure 4.13 do not present the progressive damage of FRP rods. Therefore, it is a challenge to understand the first failure phase of FRP rods.



(a) GFRP rod failure [81]



(b) CFRP rod failure [76]

Figure 4.12. Typical failure modes of GFRP and CFRP rods.

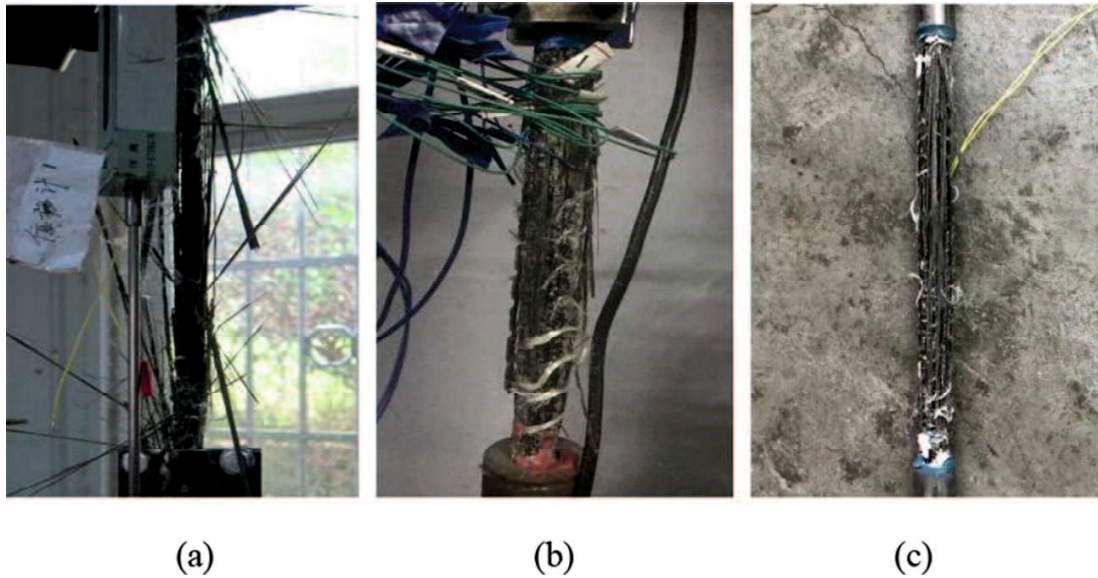


Figure 4.13. Typical failure modes of BFRP rods [87].

The progressive damage of FRP rods was shown in videos [88–90]. The first phase of the failure is generally in the longitudinal direction (mode c), and then the failure occurs in both modes (a) and (c) from the second phase to the last phase in a short time [88,89]. The FRP rods could only be ruptured in the transverse direction in cases [90], and in Figure 4.13 (c). The failure of FRP rods appears in the matrix with the delamination phenomenon. The fibers do not fail in such cases. Therefore, the first phase of failure is the key role of the FRP rod failure. If the first phase occurs in mode (a), the other phases will appear in mode (a). However, if the first phase is in mode (c), the other phases are both in modes (a) and (c).

Table 10. Predicted results of AFRP rods.

Table 10 (a). Diameter  $d=3\text{mm}$

Cases*	Load-capacity (kN)				Rod failure behavior	Averaged load-capacity (kN)
	FC-1	FC-2	FC-3	FC-4		
D3-60-1	-	-	-	-	Unruptured	14.8
D3-60-2	-	-	-	-	Unruptured	
D3-60-4	-	-	-	-	Unruptured	
D3-60-6	-	-	-	-	Unruptured	
D3-60-8	-	-	-	-	Unruptured	
D3-70-1	14.3 (a)**	15.1 (c)	15.1 (c)	15.1 (c)	Ruptured	
D3-70-2	14.5 (a)	15.1 (c)	15.1 (c)	15.1 (c)	Ruptured	
D3-70-4	14.6 (a)	15.2 (c)	15.2 (c)	15.2 (c)	Ruptured	
D3-70-6	13.4 (a)	15.0 (c)	15.0 (c)	15.0 (c)	Ruptured	
D3-70-8	13.4 (a)	14.9 (c)	14.9 (c)	14.9 (c)	Ruptured	

\* D3-60-1 denotes that diameter (3 mm), maximum tangential stress (60 MPa), and displacement ratio ( $R_d=1$ ).

\*\* (a) and (c) denote the failure modes in Table 4.

Table 10 (b). Diameter  $d=4$  mm

Cases*	Load-capacity (kN)				Rod failure behavior	Averaged load-capacity (kN)
	FC-1	FC-2	FC-3	FC-4		
D4-60-1	-	-	-	-	Unruptured	26.0
D4-60-2	-	-	-	-	Unruptured	
D4-60-4	-	-	-	-	Unruptured	
D4-60-6	23.4 (a)	27.3 (c)	27.3 (c)	27.3 (c)	Ruptured	
D4-60-8	24.1 (a)	26.6 (a)	27.4 (c)	27.4 (c)	Ruptured	
D4-70-1	22.0 (a)	26.7 (c)	26.7 (c)	26.7 (c)	Ruptured	
D4-70-2	21.4 (a)	26.8 (c)	26.8 (c)	26.8 (c)	Ruptured	
D4-70-4	22.4 (a)	27.1 (c)	27.1 (c)	27.1 (c)	Ruptured	
D4-70-6	22.8 (a)	27.0 (c)	28.0 (c)	29.0 (c)	Ruptured	
D4-70-8	22.3 (a)	26.9 (c)	26.9 (c)	26.9 (c)	Ruptured	

\* D4-60-1 denotes that diameter (4 mm), maximum tangential stress (60 MPa), and displacement ratio ( $R_d=1$ ).

\*\* (a) and (c) denote the failure modes in Table 4.

Table 10 (c). Diameter  $d=6$  mm

Cases*	Load-capacity (kN)				Rod failure behavior	Averaged load-capacity (kN)
	FC-1	FC-2	FC-3	FC-4		
D6-60-1	-	-	-	-	Unruptured	
D6-60-2	43.9 (a)	49.2 (a)	55.7 (a)	58.7 (a)	Ruptured	
D6-60-4	46.7 (a)	55.7 (a)	59.3 (a)	59.9 (c)	Ruptured	
D6-60-6	46.1 (a)	54.1 (a)	59.6 (a)	60.3 (c)	Ruptured	
D6-60-8	45.6 (a)	53.2 (a)	59.6 (a)	60.4 (c)	Ruptured	
D6-70-1	42.5 (a)	56.1 (a)	59.2 (c)	59.2 (c)	Ruptured	54.7
D6-70-2	43.3 (a)	56.7 (a)	59.3 (c)	59.3 (c)	Ruptured	
D6-70-4	43.5 (a)	58.5 (a)	59.2 (c)	59.2 (c)	Ruptured	
D6-70-6	44.9 (a)	58.2 (a)	59.5 (c)	59.5 (c)	Ruptured	
D6-70-8	42.9 (a)	59.5 (a)	59.5 (c)	59.5 (c)	Ruptured	

\* D6-60-1 denotes that diameter (6 mm), maximum tangential stress (60 MPa), and displacement ratio ( $R_d=1$ ).

\*\* (a) and (c) denote the failure modes in Table 4.

Table 10 (d). Diameter  $d=8$  mm

Cases*	Load-capacity (kN)				Rod failure behavior	Averaged load-capacity (kN)
	FC-1	FC-2	FC-3	FC-4		
D8-60-1	-	-	-	-	Unruptured	
D8-60-2	71.7 (a)	86.6 (a)	91.7 (a)	98.6 (a)	Ruptured	
D8-60-4	72.7 (a)	85.7 (a)	93.3 (a)	105.5 (c)	Ruptured	
D8-60-6	73.3 (a)	82.7 (a)	97.2 (a)	106.4 (c)	Ruptured	
D8-60-8	73.7 (a)	82.8 (a)	97.3 (a)	106.2 (c)	Ruptured	
D8-70-1	73.4 (a)	83.5 (a)	103.5 (c)	104.3 (c)	Ruptured	92.1
D8-70-2	72.5 (a)	96.8 (a)	104.8 (c)	104.8 (c)	Ruptured	
D8-70-4	75.9 (a)	99.4 (a)	104.6 (c)	104.6 (c)	Ruptured	
D8-70-6	71.6 (a)	100.0 (a)	104.5 (c)	104.5 (c)	Ruptured	
D8-70-8	72.2 (a)	101.3 (a)	104.1 (c)	104.1 (c)	Ruptured	

\* D8-60-1 denotes that diameter (8 mm), maximum tangential stress (60 MPa), and displacement ratio ( $R_d=1$ ).

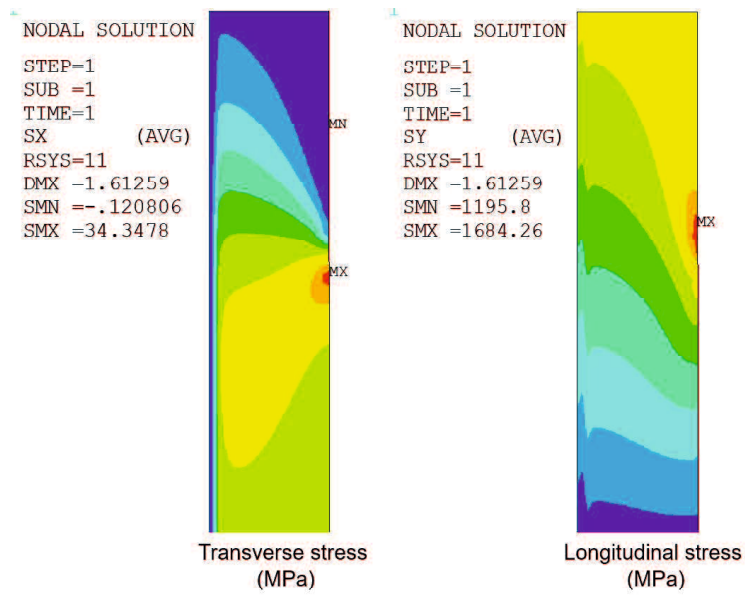
\*\* (a) and (c) denote the failure modes in Table 4.

As expected, the damage of FRP rods mainly occurs in modes (a) and (c) relating to transverse and longitudinal strengths, respectively. According to Table 10 (a-d), the failure does not happen in some FRP rods (D3, D4, D6, and D8) at interfacial tangential strength 60 MPa. Instead, the damage of these models occurs at the interfaces between the FRP rods and filling material. It is due to the fact that the interfacial tangential strength is insufficient to transfer tensile stress from the steel tubes. With an increase of interfacial strength from 60 MPa to 70 MPa, the deviation of the load-capacity between two groups is unremarkable, with diameters  $D < 8$  mm. However, group D8-70 shows higher ultimate tensile forces than group D8-60 with conditions from FC-2 to FC-4. However, the deviation within 10% is negligible.

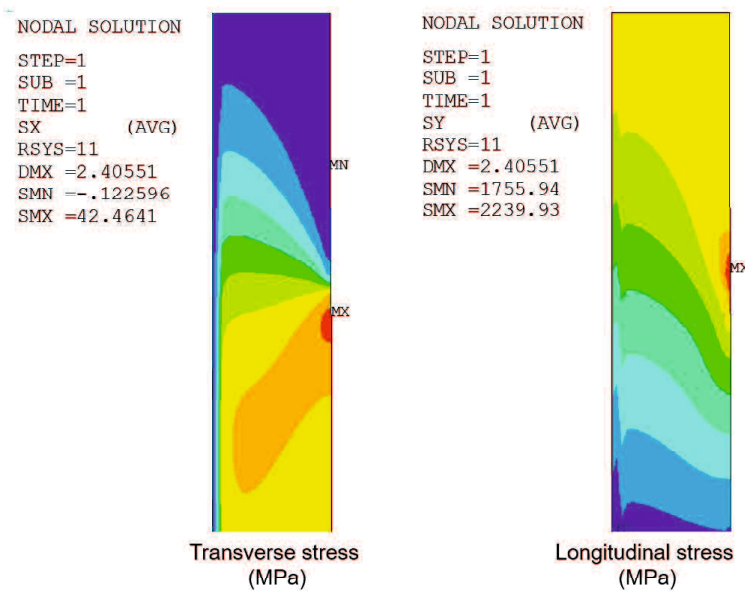
It means that the interface strength of filling materials has little influence on the load-capacity of FRP rods.

To examine the effect of interfacial fracture energy, the maximum tangential separation was varied with displacement ratios from 1 to 8. Each group with similar interface strength is investigated with each failure criterion. For instance, in group D6-60 with FC-1 criterion, the deviations among ultimate tensile forces are not significant, under 7%. Similar trends are found in the other groups. Therefore, the fracture energy has little effect on the load-capacity of FRP rods.

Failure criteria were established from the hypothesis of fiber-matrix interfacial strengths in the RVE-2 models. As a result, the transverse tensile strength increases from criterion FC-1 to FC-4. Based on Table 10 (a-d), the failures of the FRP rods happens in two modes (a) and (c), which denote the failures under transverse and longitudinal tension, respectively. Figure 4.14 shows an example of failure modes of the FRP rod D6-70-2. The FRP rod in the case FC-1 is ruptured in mode (a) as the maximum transverse stress reaches the transverse strength 34.2 MPa, as shown in Figure 4.14 (a). However, the maximum longitudinal stress 1684.3 MPa is much lower than the longitudinal strength 2238 MPa. In the case FC-3 in Figure 4.14 (b), the FRP rod is ruptured as the maximum longitudinal stress reaches the longitudinal strength 2238 MPa. The maximum transverse stress 42.5 MPa is lower than the strength 47.9 MPa. It means that the FRP rod remains stable in the transverse direction in this case. The load-capacity of the FRP rod D6-70-2 in the case FC-1 43.3 kN is lower than that of 59.3 kN in the case FC-3. Hence, the FRP rods do not optimize the load-capacity in mode (a).



(a) Failure in mode (a) in the case FC-1



(b) Failure in mode (c) in the case FC-3

Figure 4.14. Failure modes of the AFRP rod D6-70-2.

The increase in the transverse tensile strength (from FC-1 to FC-4) is directly proportional to the load-capacity. For instance, the ultimate tensile force of D8-60-2 in Table

10 (d) increases from 71.7 to 98.6 kN as the transverse tensile strength increases from 34.2 to 52.3 MPa (from FC-1 to FC-4). However, the increase has no effect on the load-capacity as transverse tensile strength is barely adequate to keep stability in the transverse direction. As expected, the failure of the FRP rods is now dependent on the longitudinal tensile strength. For example, as seen in D8-70-1 data with failure mode (a), the load-capacity increase from 73.4 to 83.5 kN with an increase of the transverse tensile strength from 34.2 (FC-1) to 41.3 MPa (FC-2). However, the load-capacity remains constant at about 104.0 kN as the transverse tensile strength is more than or equal to 47.9 MPa in cases (FC-3 and FC-4). The failure occurs in mode (c) in such cases. It means that mode (c) is the most optimized state of the failure with the maximum load-capacity of the FRP rods.

With groups D3 and D4, the failures happen in mode (a) relating to criterion (FC-1) and mode (c) relating to criteria (FC-2, FC-3, and FC-4). By contrast, groups D6 and D8 show another trend of failure modes, with mode (a) relating to criteria (FC-1 and FC-2) and mode (c) relating to criteria (FC-3 and FC-4). Moreover, mode (a) sometimes appears in criteria FC-3 and FC-4 in D6 and D8 groups. For instance, with a similar transverse tensile strength in the criterion FC-2, while the FRP rods (D6 and D8) are ruptured in mode (a), the FRP rods (D3 and D4) maintain stability in the transverse direction and show damage in mode (c). The data suggest that the increase in diameter is directly proportional to the damage in the transverse direction.

Table 11. Comparison of results.

D (mm)	Load-capacity $P_u$ (kN)			Deviation (%)	
	Specified	Experimental	Predicted	Spe-Pre *	Exp-Pre *
3	13.0	N/A	14.8	13.8	N/A
4	22.7	N/A	26.0	14.5	N/A
6	49.9	53.1	54.7	9.6	3.0
8	86.1	90.0	92.1	7.0	2.3

\* Spe, Exp, and Pre denote the specified, experimental, and predicted load, respectively.

Table 11 shows the comparison of computational results of the present study with specified and experimental results [36]. The deviations between specified and predicted

results are remarkable. However, the specified ultimate tensile forces proposed for the design are lower than the actual ones. The predicted ultimate tensile forces are consistent with experimental ones, with a deviation from 2.3 to 3%.

Moreover, McKay and Erki [77] showed that the Technora FRP rod ( $d=6$  mm) was not ruptured at a tensile force of 53.2 kN. Similarly, in an experiment, the Technora FRP rod ( $d=8$  mm) was not ruptured at a pull-out force of 91.67 kN [78]. The results in studies [77,78] approximate experimental values in Table 11. The data indicate that the load-capacity of FRP rods (D6 and D8) could be higher than values 53.1 kN and 90 kN in the previous study [36], respectively. Predicted results in Table 10 with approximately 60 kN (D6) and 104 kN (D8) are acceptable in such cases. It means that present FE models are effective for predicting the load-capacity of FRP rods.

#### **4.3.2. Shear-lag effect**

The free section and failure section in the free length and sensitive area were investigated, respectively. Figure 4.15 shows the equal distribution of longitudinal tensile stress from FC-1 to FC-3 in free sections. It means that the shear-lag effect does not affect the free sections. However, the shear-lag effect causes unequal stress distribution in the failure sections of FRP rod D6-70-2 in failure modes (a) and (c). The longitudinal stresses decrease from the maximum value at the lateral surface to the minimum one at the core of the FRP rod, with a reduction from 10 to 15%.

Three curves of longitudinal stress distribution in failure sections from FC-1 to FC-3 parallel with each other in Figure 4.15. It suggests that the shear-lag effect exists in failure sections in both modes (a) and (c). Both maximum longitudinal tensile stresses 1659 MPa in FC-1 and 2126 MPa in FC-2 are lower than the longitudinal tensile strength 2238 MPa in mode (a). The failure of FRP rods occurs in the transverse direction in such a case. The longitudinal load-capacity will not be affected by the shear-lag effect in mode (a). Consequently, the shear-lag effect only impacts mode (c) in which the damage is specified in the longitudinal tensile stress.

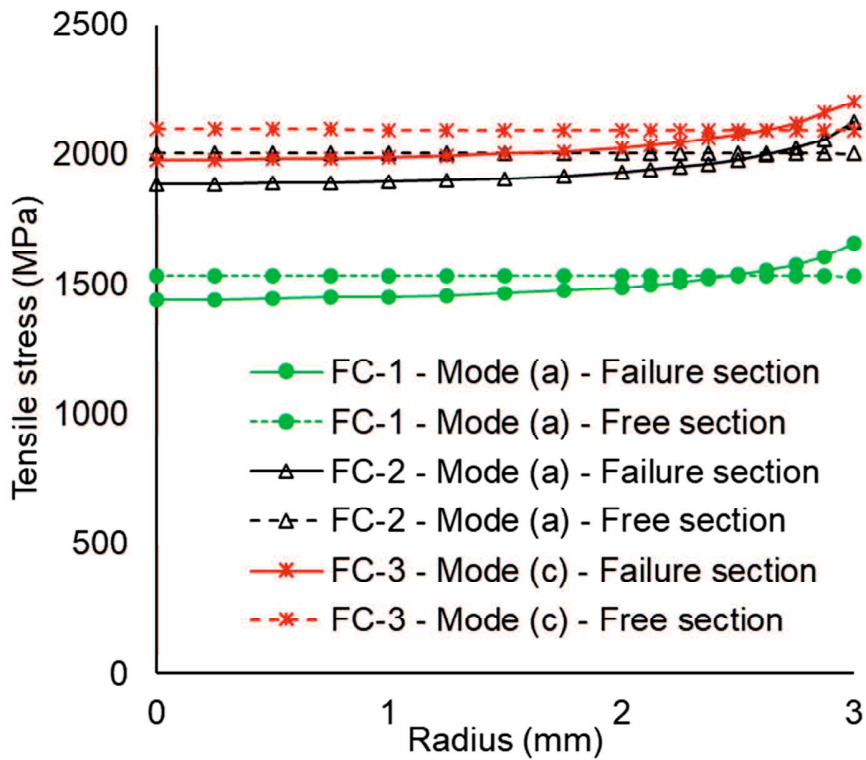


Figure 4.15. Longitudinal tensile stress distribution in cross-sections of AFRP rod D6-70-2.

To quantify the diameter effect, the stress distribution with various rod diameters is investigated and reported in Figure 4.16. The analysis in this step is based on the failure mode (c). All curves are rearranged on the coordinate system of FRP rod D8. As shown in Figure 4.16, all curves peak the highest value 2238 MPa at the lateral surfaces of FRP rods. The FRP rods (D3, D4, and D6) have a similar trend in stress distribution. The FRP rod D8 shows a higher decrease than other rods. Consequently, the rise in the diameter is directly proportional to the increase of the shear-lag effect.

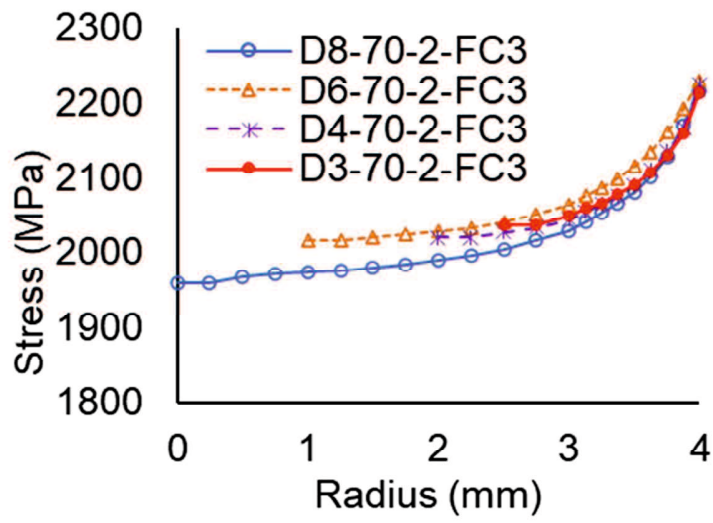
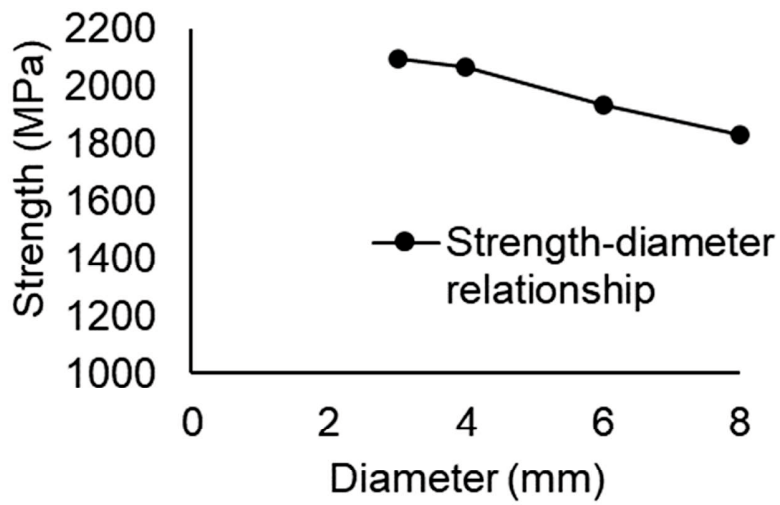
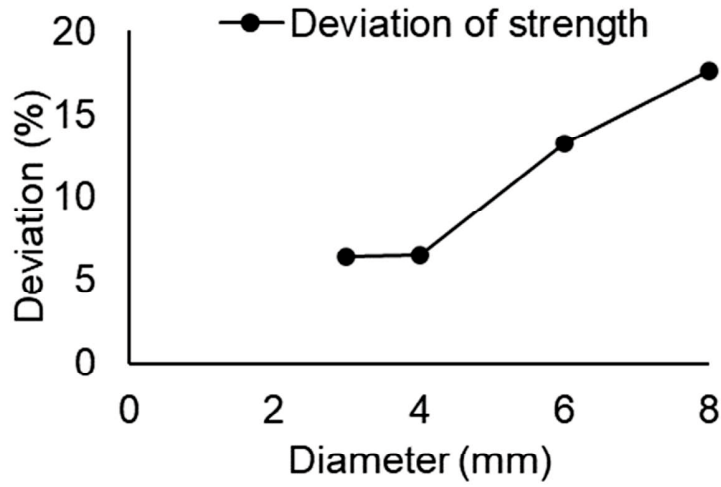


Figure 4.16. Stress distribution in FRP rods with various diameters.



(a) Strength reduction



(b) Deviation of tensile strength

Figure 4.17. Effect of the shear-lag in various AFRP rods.

The tensile strength of each FRP rod was calculated from the average load-capacity in Table 10 (a-d) as follows Equation (28). The strength-diameter relationship was presented in Figure 4.17 (a).

$$\sigma_u^{rod} = P_u / A_{rod} \quad (28)$$

where  $\sigma_u^{rod}$ ,  $P_u$ , and  $A_{rod}$  are the tensile strength, load-capacity, and cross-section area of each FRP rod, respectively.

The tensile strength of FRP rods decreases from around 2094 MPa (D3) to around 1832 MPa (D8). Without the shear-lag effect, the tensile strength of FRP rods can reach 2238 MPa. The deviation between the tensile strengths of each FRP rod and FRP material 2238 MPa depends on the shear-lag effect. The deviation increases from about 6 to 18% with the rise in diameter from 3 to 8 mm, as shown in Figure 4.17 (b). It means that the shear-lag effect in a

large diameter is higher than that in a small diameter. The increase of the shear-lag effect reduces the tensile strength of FRP rods. Moreover, the load-capacity following Equation (28) is lower than the theoretical value. Therefore, the diameter is a significant factor that affects the shear-lag effect and longitudinal tensile strength, and load-capacity of FRP rods.

## Chapter 5. Discussion

### 5.1. Comparison of models A, B, and C

The present study suggested modes B and C to compare with mode A. The tensile stress at failure sections of all three models was compared in detail. As shown in Figure 5.1, the gradient decrease in modes B and C is higher than that of mode A at the outer region. In addition, model C shows relatively higher tensile stress at the core of the FRP rod compared to modes A and B. Therefore, the behavior of model A is different from the behavior of models B and C in the tensile models of FRP rods. Consequently, the assumption of transversely isotropic FRP rods as isotropic materials in the previous study [44] is incorrect in such a case. In addition, the suggestion of transversely isotropic fibers as isotropic fibers in the previous study [85] is inappropriate. Therefore, the transversely isotropic of fibers should be calculated in predicting the FRP materials.

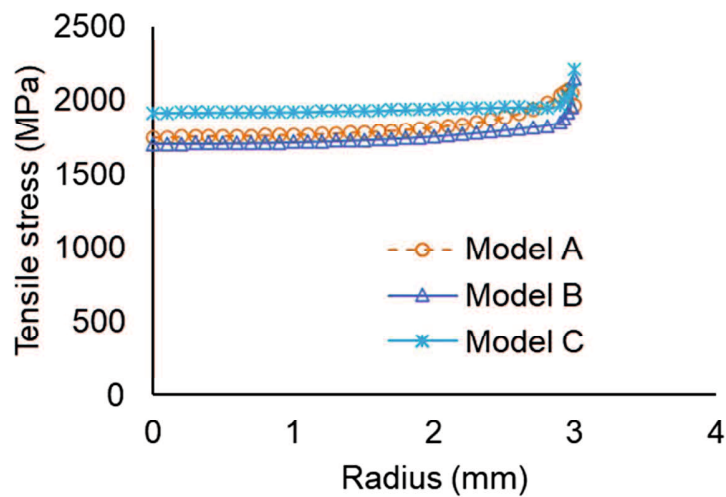


Figure 5.1. Tensile stress at failure sections of models A, B, and C (D6).

## 5.2. Shear-lag effect

A remarkable finding in the present study is the shear-lag effect in FRP rods. As presented in sections 4.2.1 and 4.3.2, the study has confirmed the shear-lag effect introduced in the previous study [42]. In addition, the shear-lag was demonstrated by numerical models with various cases of bond performance between FRP rods and the filling material. Figure 5.2 shows a comparison of the shear-lag effect in various conditions.

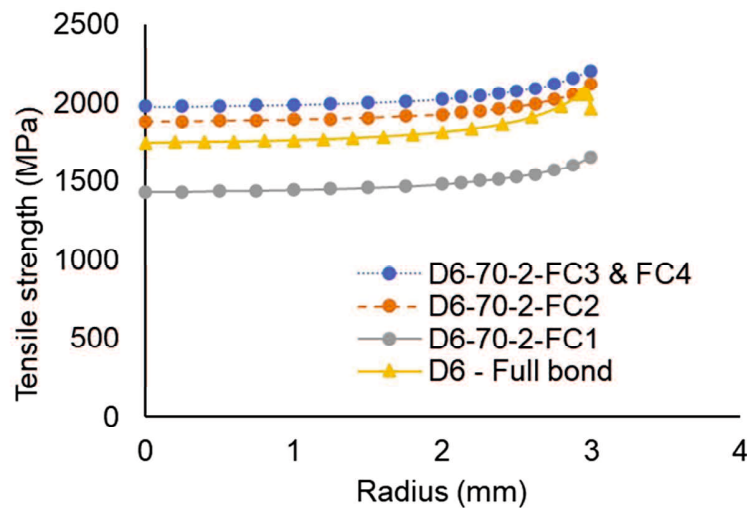


Figure 5.2. Shear-lag effect between the full-bonding and partially-bonding strength (D6).

The shear-lag effect always exists at the failure sections of FRP rods. The deviation between the maximum and minimum of tensile stress of model D6 – full-bonding is approximately 16%. It is higher than the other cases in Figure 5.2, from about 10 to 13%. The gradient decrease of tensile stress in the full-bonding model is higher than that of others. The stress concentration may explain the results at the failure section in the full-bonding model.

As discussed in section 4.3.2, the shear-lag effect impacts the tensile strength of FRP rods if the failure occurs in mode (c). It means that the FRP rods are ruptured by the longitudinal tensile strength of material 2238 MPa. Therefore, the study compares the full-bonding FRP models with partially-bonding strength models in mode (c). Figure 4.6 shows the stress distribution in the failure section of full-bonding FRP rods with various diameters.

Figure 4.16 presents tensile stress distribution in FRP rods damaged in mode (c). All curves in Figure 4.6 show a similar trend of the stress distribution. By contrast, curve D8 has a more significant decrease in stress than the other diameters in Figure 4.16. The full-bonding model is similar to the partially-bonding model in such cases of diameter from 3 to 6 mm. The full-bonding model is an unreal assumption. However, it could be applied for small diameters. Consequently, the partially-bonding strength model is recommended for UD FRP rods.

**5.3. Diameter effects**

Previous studies [37–42] implied that the shea-lag effect reduces the strength of FRP rods. However, there was no evidence for this argument. To quantify the shear-lag effect, the study investigates the strength of various diameters, as shown in Figure 5.3. Predicted results are relatively similar to the specified and experimental strengths. The specified strength is lower than the other strengths. It is explained that the specified strength is utilized for design and requires a consideration of a safety factor.

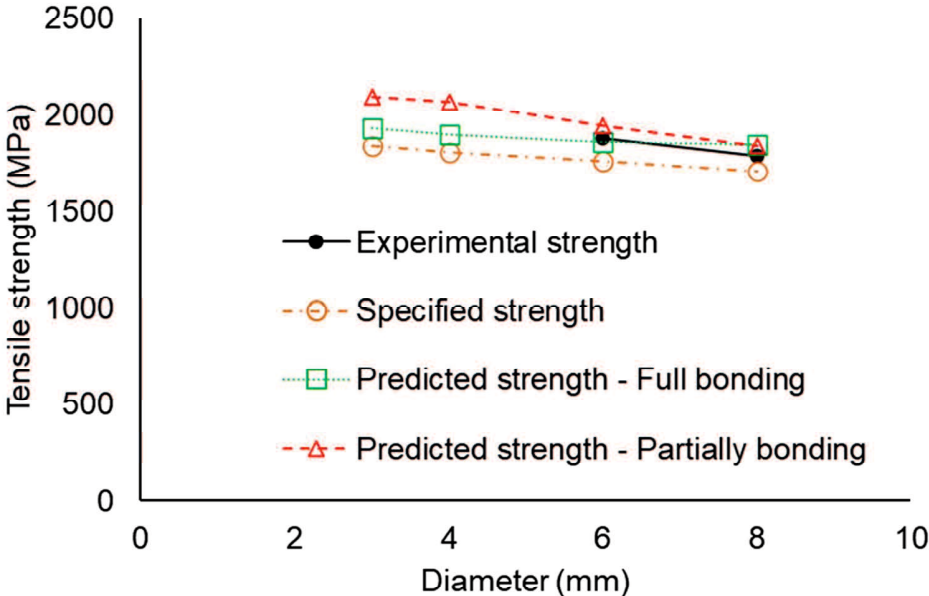


Figure 5.3. Tensile strength reduction with the diameter.

The increase in the diameter induces a decrease in tensile strength. As shown in Figure 4.6 and Figure 4.16, the maximum tensile strengths of all curves from D3 to D8 are similar at the lateral surface of FRP rods. However, the deviation between the maximum and minimum values on each curve increase with the diameter. It means that the shear-lag in a large diameter is higher than that in a small diameter. It causes the reduction of strength in large diameter. The present study has demonstrated the argument in previous studies [37–42] in detail.

## Chapter 6. Conclusions and recommendations

### 6.1. Conclusions

The study aimed at determining tensile properties of pultruded FRP rods made of Technora fibers 65% and vinyl ester resin 35%. All mechanical properties of FRP elements were predicted by the simulation using the RVE-1 model. Moreover, a numerical model, RVE-2, was proposed to predict tensile strengths of AFRP material in 3D directions to validate the tensile failure of FRP rods. The following conclusions can be drawn:

- The present findings indicate the existence of the shear-lag effect and the failure section in the FRP rod by numerical simulation. It also clearly demonstrates the shear-lag phenomenon referenced in Achillides et al. [42] and Firas et al. [43]. The failure section is much more damaged than other cross-sections, and the FRP rod must be ruptured at this section.
- The shear-lag effect only causes the nonlinear distribution of the axial tensile stress in the cross-sections close to the anchorage. The stress profiles in the failure sections of all diameters include two phases: significantly decreasing in outermost layers and slightly declining in the other layers. The present study indicates that the increase of the diameter induces the decrease of the tensile strength. Moreover, it was confirmed that the partially-bonding strength model is more appropriate than the full-bonding model.
- Properties of the interfaces between the FRP rods and filling material, including bond strength and fracture energy, show little effect on failure modes in the partially-bonding strength model.
- The tensile strengths of FRP material should be applied to investigate the failure of FRP rods. The results indicated two failure modes of FRP rods under tension, including transverse and longitudinal directions. The failure modes are the most significant factor affecting the load-capacity of FRP rods. However, the failure criteria should be applied for the partially-bonding strength model in which the transverse tensile stress in FRP rods is caused by appropriate bond strength. By contrast, the full-bonding model shows fixed contact between FRP rods that induced high transverse tensile strength in FRP

rods. Therefore, the full-bonding model only employed the longitudinal tensile strength as the failure index.

- The transverse tensile strength is a significant factor needed to be investigated in designing FRP rods. FRP rods must have enough transverse tensile strength to induce the damage in the longitudinal direction. The damage in the transverse direction is directly proportional to the increase of the rod diameter.
- Numerical simulation models can be applied to predict failure modes and the load-capacity of FRP rods. The deviations between the simulation and experimental results are unremarkable. Note is that the properties of FRP materials in the global models have to be consistent with ones predicted from RVE models.

## **6.2. Recommendations for future works**

Most FRP rods show higher tensile strength than standard steel. The FRP rods are often used to strengthen tensile areas in concrete structures. Therefore, the tensile ability is the most important factor of FRP rods. The present study has shown some advantages in predicting the tensile properties of FRP materials, the failure modes, the shear-lag effect, and the ultimate tensile forces of FRP rods. However, some further studies should be conducted to investigate as follows.

- The FRP rods in this study were made of 65% aramid fibers and 35% vinyl ester resin. The tensile and shear properties of the FRP material were demonstrated as the linear material. However, if the volume fraction of fibers is lower than 65%, the properties of the FRP material depend on the matrix properties. Therefore, the FRP material could show nonlinear behavior in such a case. Moreover, most previous studies and commercial software (such as ANSYS) assumed that orthotropic and transversely isotropic materials are linear in three dimensions. Consequently, designing a new model with nonlinear behavior in three dimensions is required to determine whether the failure occurs in FRP rods or not.
- The present study investigated FRP rods under the static load. Therefore, further researches on dynamic behavior of FRP rods should be examined and assessed in the numerical simulations in future studies.

## References

- [1] Y.H.M. Amran, R. Alyousef, R.S.M. Rashid, H. Alabduljabbar, C.C. Hung, Properties and applications of FRP in strengthening RC structures: A review, *Structures*. 16 (2018) 208–238. doi:10.1016/j.istruc.2018.09.008.
- [2] ACI 440 R-96, State-of-the-art report on fiber reinforced Plastic (FRP) for concrete structures (Reapproved 2002), Farmington Hills, MI, USA, 2002.
- [3] C. Acquah, I. Datskov, A. Mawardi, F. Zhang, L.E.K. Achenie, R. Pitchumani, E. Santos, Optimization under uncertainty of a composite fabrication process using a deterministic one-stage approach, *Comput. Chem. Eng.* 30 (2006) 947–960. doi:10.1016/j.compchemeng.2005.12.015.
- [4] X.L. Zhao, L. Zhang, State-of-the-art review on FRP strengthened steel structures, *Eng. Struct.* 29 (2007) 1808–1823. doi:10.1016/j.engstruct.2006.10.006.
- [5] D. Schnerch, M. Dawood, S. Rizkalla, E. Sumner, Proposed design guidelines for strengthening of steel bridges with FRP materials, *Constr. Build. Mater.* 21 (2007) 1001–1010. doi:10.1016/j.conbuildmat.2006.03.003.
- [6] K.A. Harries, A.J. Peck, E.J. Abraham, Enhancing stability of structural steel sections using FRP, *Thin-Walled Struct.* 47 (2009) 1092–1101. doi:10.1016/j.tws.2008.10.007.
- [7] P. Colombi, G. Fava, L. Sonzogni, Fatigue crack growth in CFRP-strengthened steel plates, *Compos. Part B Eng.* 72 (2015) 87–96. doi:10.1016/j.compositesb.2014.11.036.
- [8] J.G. Teng, T. Yu, D. Fernando, Strengthening of steel structures with fiber-reinforced polymer composites, *J. Constr. Steel Res.* 78 (2012) 131–143. doi:10.1016/j.jcsr.2012.06.011.
- [9] J.W. Schmidt, A. Bennitz, B. Täljsten, P. Goltermann, H. Pedersen, Mechanical anchorage of FRP tendons - A literature review, *Constr. Build. Mater.* 32 (2012) 110–121. doi:10.1016/j.conbuildmat.2011.11.049.
- [10] S.A. Youakim, V.M. Karbhari, An approach to determine long-term behavior of concrete members prestressed with FRP tendons, *Constr. Build. Mater.* 21 (2007) 1052–1060. doi:10.1016/j.conbuildmat.2006.02.006.

- [11] X. Wang, J. Shi, G. Wu, L. Yang, Z. Wu, Effectiveness of basalt FRP tendons for strengthening of RC beams through the external prestressing technique, *Eng. Struct.* 101 (2015) 34–44. doi:10.1016/j.engstruct.2015.06.052.
- [12] T. Lou, S.M.R. Lopes, A. V. Lopes, Numerical analysis of behaviour of concrete beams with external FRP tendons, *Constr. Build. Mater.* 35 (2012) 970–978. doi:10.1016/j.conbuildmat.2012.04.055.
- [13] T. Lou, S.M.R. Lopes, A. V. Lopes, A comparative study of continuous beams prestressed with bonded FRP and steel tendons, *Compos. Struct.* 124 (2015) 100–110. doi:10.1016/j.compstruct.2015.01.009.
- [14] L.-Z. Yao, G. Wu, Fiber-element modeling for seismic performance of square RC bridge columns retrofitted with NSM BFRP bars and/or BFRP sheet confinement, *J. Compos. Constr.* 20 (2016) 04016001.(1–15). doi:10.1061/(ASCE)CC.1943-5614.0000652.
- [15] F. Elgabbas, P. Vincent, E.A. Ahmed, B. Benmokrane, Experimental testing of basalt-fiber-reinforced polymer bars in concrete beams, *Compos. Part B Eng.* 91 (2016) 205–218. doi:10.1016/j.compositesb.2016.01.045.
- [16] B. Benmokrane, O. Chaallal, R. Masmoudi, Flexural response of concrete beams reinforced with FRP reinforcing bars, *ACI Struct. J.* 93 (1996) 46–55. doi:10.14359/9839.
- [17] M. Komuro, Y. Kurihashi, T. Kawarai, N. Kishi, Numerical simulation of AFRP Rod NSM RC beams under falling-weight impact loading, in: *Am. Concr. Institute, ACI Spec. Publ.*, 2017: pp. 17.(1–14).
- [18] R. Capozucca, On the strengthening of RC beams with near surface mounted GFRP rods, *Compos. Struct.* 117 (2014) 143–155. doi:10.1016/j.compstruct.2014.06.030.
- [19] L. De Lorenzis, J.G. Teng, Near-surface mounted FRP reinforcement: An emerging technique for strengthening structures, *Compos. Part B Eng.* 38 (2007) 119–143. doi:10.1016/j.compositesb.2006.08.003.
- [20] A. Rizzo, L. De Lorenzis, Modeling of debonding failure for RC beams strengthened in shear with NSM FRP reinforcement, *Constr. Build. Mater.* 23 (2009) 1568–1577. doi:10.1016/J.CONBUILDMAT.2008.03.009.
- [21] B. Benmokrane, O. Chaallal, R. Masmoudi, Glass fibre reinforced plastic (GFRP)

- rebars for concrete structures, *Constr. Build. Mater.* 9 (1995) 353–364. doi:10.1016/0950-0618(95)00048-8.
- [22] I.A. Sharaky, L. Torres, J. Comas, C. Barris, Flexural response of reinforced concrete (RC) beams strengthened with near surface mounted (NSM) fibre reinforced polymer (FRP) bars, *Compos. Struct.* 109 (2014) 8–22. doi:10.1016/j.compstruct.2013.10.051.
- [23] H. Zhu, S. Cheng, D. Gao, S.M. Neaz, C. Li, Flexural behavior of partially fiber-reinforced high-strength concrete beams reinforced with FRP bars, *Constr. Build. Mater.* 161 (2018) 587–597. doi:10.1016/j.conbuildmat.2017.12.003.
- [24] C. Barris, L. Torres, J. Comas, C. Miàs, Cracking and deflections in GFRP RC beams: An experimental study, *Compos. Part B Eng.* 55 (2013) 580–590. doi:10.1016/j.compositesb.2013.07.019.
- [25] C.K.Y. Leung, Z. Chen, S. Lee, M. Ng, M. Xu, J. Tang, Effect of size on the failure of geometrically similar concrete beams strengthened in shear with FRP strips, *J. Compos. Constr.* 11 (2007) 487–496. doi:10.1061/(asce)1090-0268(2007)11:5(487).
- [26] J. Yao, J.G. Teng, J.F. Chen, Experimental study on FRP-to-concrete bonded joints, *Compos. Part B Eng.* 36 (2005) 99–113. doi:10.1016/j.compositesb.2004.06.001.
- [27] S.S. Zhang, T. Yu, G.M. Chen, Reinforced concrete beams strengthened in flexure with near-surface mounted (NSM) CFRP strips: Current status and research needs, *Compos. Part B Eng.* 131 (2017) 30–42. doi:10.1016/j.compositesb.2017.07.072.
- [28] J.H. Lee, M.M. Lopez, C.E. Bakis, Slip effects in reinforced concrete beams with mechanically fastened FRP strip, *Cem. Concr. Compos.* 31 (2009) 496–504. doi:10.1016/j.cemconcomp.2009.04.008.
- [29] S.K. Woo, J.W. Nam, J.H.J. Kim, S.H. Han, K.J. Byun, Suggestion of flexural capacity evaluation and prediction of prestressed CFRP strengthened design, *Eng. Struct.* 30 (2008) 3751–3763. doi:10.1016/j.engstruct.2008.06.013.
- [30] J.G. Teng, S.S. Zhang, J.F. Chen, Strength model for end cover separation failure in RC beams strengthened with near-surface mounted (NSM) FRP strips, *Eng. Struct.* 110 (2016) 222–232. doi:10.1016/j.engstruct.2015.11.049.
- [31] ACI PRC-440.1-15, Guide for the Design and Construction of Structural Concrete Reinforced with Fiber-Reinforced Polymer Bars, Farmington Hills, MI, USA, 2015.
- [32] FIB Bulletin No. 40, FRP reinforcement in RC structures, fib. The International

Federation for Structural Concrete, 2007. doi:10.35789/fib.BULL.0040.

- [33] ACI 440.2R-08, Guide for the design and construction of externally bonded FRP systems for strengthening concrete structures, Farmington Hills, 2008.
- [34] O. Corning Composite Solutions, ASLAN™ 100 Glass fiber reinforced polymer (GFRP) rebars for infrastructure solutions, 2017. <http://composites.owenscorning.com> (accessed November 27, 2019).
- [35] Kodiak Rebar, Fiberglass rebar (GFRP) glass fiber reinforced polymer, (2019). <https://www.fiberglassrebar.us/> (accessed November 27, 2019).
- [36] K. Noritake, R. Kakihara, S. Kumagai, J. Mizutani, Technora, an aramid FRP rod, *Fiber-Reinforced-Plastic Reinf. Concr. Struct.* (1993) 267–290. doi:10.1016/B978-0-444-89689-6.50016-1.
- [37] B. Benmokrane, A. Manalo, J.-C. Bouhet, K. Mohamed, M. Robert, Effects of diameter on the durability of glass fiber–reinforced polymer bars conditioned in alkaline solution, *J. Compos. Constr.* 21 (2017) 4017040.(1–12). doi:10.1061/(ASCE)CC.1943-5614.0000814.
- [38] C. Li, D. Gao, Y. Wang, J. Tang, Effect of high temperature on the bond performance between basalt fibre reinforced polymer (BFRP) bars and concrete, *Constr. Build. Mater.* 141 (2017) 44–51. doi:10.1016/j.conbuildmat.2017.02.125.
- [39] G.B. Maranan, A.C. Manalo, W. Karunasena, B. Benmokrane, Pullout behaviour of GFRP bars with anchor head in geopolymer concrete, *Compos. Struct.* 132 (2015) 1113–1121. doi:10.1016/j.compstruct.2015.07.021.
- [40] H. Wang, X. Sun, G. Peng, Y. Luo, Q. Ying, Experimental study on bond behaviour between BFRP bar and engineered cementitious composite, *Constr. Build. Mater.* 95 (2015) 448–456. doi:10.1016/j.conbuildmat.2015.07.135.
- [41] A. Kalamkarov, G. Saha, S. Rokkam, J. Newhook, A. Georgiades, Strain and deformation monitoring in infrastructure using embedded smart FRP reinforcements, *Compos. Part B Eng.* 36 (2005) 455–467. doi:<https://doi.org/10.1016/j.compositesb.2004.12.003>.
- [42] Z. Achillides, K. Pilakoutas, Bond behavior of fiber reinforced polymer bars under direct pullout conditions, *J. Compos. Constr.* 8 (2004) 519–527. doi:10.1061/(ASCE)1090-0268(2004)8:2(173).

- [43] F. Sayed Ahmad, G. Foret, R. Le Roy, Bond between carbon fibre-reinforced polymer (CFRP) bars and ultra high performance fibre reinforced concrete (UHPFRC): Experimental study, *Constr. Build. Mater.* 25 (2011) 479–485. doi:10.1016/J.CONBUILDMAT.2010.02.006.
- [44] F. Puigvert, A.D. Crocombe, L. Gil, Static analysis of adhesively bonded anchorages for CFRP tendons, *Constr. Build. Mater.* 61 (2014) 206–215. doi:10.1016/j.conbuildmat.2014.02.072.
- [45] N. Van Vo, I. Yoshitake, Assessing shear-lag effect on pulltruded FRP rods based on a numerical simulation, *Int. J. GEOMATE.* 21 (2021) 167–176. doi:10.21660/2021.84.j2163.
- [46] E.J. Barbero, *Introduction to Composite Materials Design*, 3 rd, CRC Press, New York, 2017. doi:https://doi.org/10.1201/9781315296494.
- [47] J. Newhook, D. Svecova, Design Manual No.3-Reinforcing concrete structures with fibre reinforced polymers, *Can. Netw. Centers Excell. Intell. Sens. Innov. Struct. Manitoba Univ. Winnipeg.* (2007) 151.
- [48] J.C. Halpin, *Effects of environmental factors on composite materials*, 1969.
- [49] E.J. Barbero, *Finite Element Analysis of Composite Materials Using ANSYS*, 2nd ed., CRC Press, New York, 2014.
- [50] C.T. Sun, R.S. Vaidya, Prediction of composite properties from a representative volume element, *Compos. Sci. Technol.* 56 (1996) 171–179. doi:10.1016/0266-3538(95)00141-7.
- [51] J.M. Whitney, M.B. Riley, Elastic properties of fiber reinforced composite materials, *AIAA J.* 4 (1966) 1537–1542. doi:10.2514/3.3732.
- [52] C.T. Sun, J.L. Chen, A micromechanical model for plastic behavior of fibrous composites, *Compos. Sci. Technol.* 40 (1991) 115–129. doi:10.1016/0266-3538(91)90092-4.
- [53] C.C. Chamis, *Simplified composite micromechanics equations for hygral, thermal and mechanical properties*, Ohio, 1983.
- [54] I. ANSYS, *ANSYS Mechanical Enterprise*, (2019).
- [55] R. Luciano, E. Sacco, Variational methods for the homogenization of periodic heterogeneous media, *Eur. J. Mech. A/Solids.* 17 (1998) 599–617. doi:10.1016/S0997-

7538(99)80024-2.

- [56] W.C. Cui, M.R. Wisnom, M. Jones, A comparison of failure criteria to predict delamination of unidirectional glass/epoxy specimens waisted through the thickness, *Composites*. 23 (1992) 158–166. doi:10.1016/0010-4361(92)90436-X.
- [57] V.D. Azzi, S.W. Tsai, Anisotropic strength of composites, *Exp. Mech.* 5 (1965) 283–288. doi:10.1007/BF02326292.
- [58] S.W. Tsai, E.M. Wu, A general theory of strength for anisotropic materials, *J. Compos. Mater.* 5 (1971) 58–80. doi:10.1177/002199837100500106.
- [59] Z. Hashin, A. Rotem, A fatigue failure criterion for fiber reinforced materials, *J. Compos. Mater.* 7 (1973) 448–464. doi:10.1177/002199837300700404.
- [60] Z. Hashin, Failure criteria for unidirectional fiber composites, *J. Appl. Mech.* 47 (1980) 329–334. doi:10.1115/1.3153664.
- [61] V. V Vasiliev, E. V Morozov, Failure criteria and strength of laminates, in: V. V Vasiliev, E. V Morozov (Eds.), *Adv. Mech. Compos. Mater.*, second ed., Elsevier Science Ltd, Oxford, 2007: pp. 321–357. doi:https://doi.org/10.1016/B978-008045372-9/50006-3.
- [62] L.E. Asp, L.A. Berglund, R. Talreja, Prediction of matrix-initiated transverse failure in polymer composites, *Compos. Sci. Technol.* 56 (1996) 1089–1097. doi:https://doi.org/10.1016/0266-3538(96)00074-7.
- [63] T.J. Vaughan, C.T. McCarthy, Micromechanical modelling of the transverse damage behaviour in fibre reinforced composites, *Compos. Sci. Technol.* 71 (2011) 388–396. doi:10.1016/j.compscitech.2010.12.006.
- [64] T.J. Vaughan, C.T. McCarthy, A micromechanical study on the effect of intra-ply properties on transverse shear fracture in fibre reinforced composites, *Compos. Part A Appl. Sci. Manuf.* 42 (2011) 1217–1228. doi:10.1016/j.compositesa.2011.05.004.
- [65] L. Yang, Y. Yan, Y. Liu, Z. Ran, Microscopic failure mechanisms of fiber-reinforced polymer composites under transverse tension and compression, *Compos. Sci. Technol.* 72 (2012) 1818–1825. doi:10.1016/j.compscitech.2012.08.001.
- [66] F.H. Bhuiyan, S.H.R. Sanei, R.S. Fertig, Predicting variability in transverse effective elastic moduli and failure initiation strengths in UD composite microstructures due to randomness in fiber location and morphology, *Compos. Struct.* 237 (2020) 111887.

doi:10.1016/j.compstruct.2020.111887.

- [67] H. Yademellat, A. Nikbakht, H. Saghafi, M. Sadighi, Experimental and numerical investigation of low velocity impact on electrospun nanofiber modified composite laminates, *Compos. Struct.* 200 (2018) 507–514. doi:10.1016/j.compstruct.2018.05.146.
- [68] I.S. Floros, K.I. Tserpes, T. Löbel, Mode-I, mode-II and mixed-mode I+II fracture behavior of composite bonded joints: Experimental characterization and numerical simulation, *Compos. Part B Eng.* 78 (2015) 459–468. doi:10.1016/j.compositesb.2015.04.006.
- [69] F. París, E. Correa, J. Canas, Micromechanical view of failure of the matrix in fibrous composite materials, *Compos. Sci. Technol.* 63 (2003) 1041–1052. doi:10.1016/S0266-3538(03)00017-4.
- [70] X.P. Xu, A. Needleman, Numerical simulations of fast crack growth in brittle solids, *J. Mech. Phys. Solids.* 42 (1994) 1397–1434. doi:10.1016/0022-5096(94)90003-5.
- [71] G. Alfano, M.A. Crisfield, Finite element interface models for the delamination analysis of laminated composites: Mechanical and computational issues, *Int. J. Numer. Methods Eng.* 50 (2001) 1701–1736. doi:10.1002/nme.93.
- [72] ASTM D7205/D7205M-06, Standard test method for tensile properties of fiber reinforced polymer matrix composite bars, 2016.
- [73] S. Kawabata, Measurement of the transverse mechanical properties of high-performance fibres, *J. Text. Inst.* 81 (1990) 432–447. doi:10.1080/00405009008658721.
- [74] M. Cheng, W. Chen, T. Weerasooriya, Mechanical properties of Kevlar® KM2 single fiber, *J. Eng. Mater. Technol.* 127 (2005) 197–203. doi:10.1115/1.1857937.
- [75] C. González, J. LLorca, Mechanical behavior of unidirectional fiber-reinforced polymers under transverse compression: Microscopic mechanisms and modeling, *Compos. Sci. Technol.* 67 (2007) 2795–2806. doi:10.1016/j.compscitech.2007.02.001.
- [76] B. Benmokrane, B. Zhang, A. Chennouf, Tensile properties and pullout behaviour of AFRP and CFRP rods for grouted anchor applications, *Constr. Build. Mater.* 14 (2000) 157–170. doi:10.1016/S0950-0618(00)00017-9.
- [77] K.S. McKay, M.A. Erki, Grouted anchorages for aramid fibre reinforced plastic

- prestressing tendons, *Can. J. Civ. Eng.* 20 (1993) 1065–1069. doi:10.1139/193-137.
- [78] A. Nanni, C.E. Bakis, E.F. O’Neil, T.O. Dixon, Performance of FRP tendon-anchor systems for prestressed concrete structures, *PCI J.* 41 (n.d.) 34–44. doi:10.15554/pcij.01011996.34.44.
- [79] J.M.M. De Kok, H.E.H. Meijer, Deformation, yield and fracture of unidirectional composites in transverse loading: 1. Influence of fibre volume fraction and test-temperature, *Compos. Part A Appl. Sci. Manuf.* 30 (1999) 905–916. doi:10.1016/S1359-835X(98)00170-5.
- [80] M.T. Pvt.Ltd, Pipe Dimension- Grade 310S, (n.d.). <https://www.mbmtubes.com/pipe-dimensions.html> (accessed December 2, 2020).
- [81] S. Kocaoz, V.A. Samaranayake, A. Nanni, Tensile characterization of glass FRP bars, *Compos. Part B Eng.* 36 (2005) 127–134. doi:10.1016/j.compositesb.2004.05.004.
- [82] F. Micelli, A. Nanni, Tensile characterization of FRP rods for reinforced concrete structures, *Mekhanika Kompoz. Mater.* 39 (2003) 445–463. doi:10.1023/A:1025638310194.
- [83] M. Goldston, A. Remennikov, M.N. Sheikh, Experimental investigation of the behaviour of concrete beams reinforced with GFRP bars under static and impact loading, *Eng. Struct.* 113 (2016) 220–232. doi:10.1016/j.engstruct.2016.01.044.
- [84] E. Atutis, J. Valivonis, M. Atutis, Experimental study of concrete beams prestressed with basalt fiber reinforced polymers under cyclic load, *Compos. Struct.* 183 (2018) 389–396. doi:10.1016/j.compstruct.2017.03.106.
- [85] N. Van Vo, I. Yoshitake, A numerical simulation of shear-lag behavior in fiber reinforced polymer (FRP) rod, in: *Proc. 6th Int. Conf. Constr. Mater.*, 2020.
- [86] A. Kessler, A. Bledzki, Correlation between interphase-relevant tests and the impact-damage resistance of glass/epoxy laminates with different fibre surface treatments, *Compos. Sci. Technol.* 60 (2000) 125–130. doi:10.1016/S0266-3538(99)00105-0.
- [87] H. Huang, B. Jia, J. Lian, W.-W. Wang, Experimental investigation on the tensile performance of resin-filled steel pipe splices of BFRP bars, *Constr. Build. Mater.* 242 (2020) 118018. doi:<https://doi.org/10.1016/j.conbuildmat.2020.118018>.
- [88] M. Testing, FRP glass fiber composite rebar tensile test -Shimadzu UHF 1000kN UTM (ASTM D7205), (n.d.).

[https://www.youtube.com/watch?v=oPFdVsiJwhM&ab\\_channel=MechanicalTesting](https://www.youtube.com/watch?v=oPFdVsiJwhM&ab_channel=MechanicalTesting)  
(accessed December 10, 2021).

- [89] B&B FRP Manufacturing inc, MSTBAR tensile test 16mm, (n.d.).  
<https://www.youtube.com/watch?v=cNFbH0JtKYU> (accessed December 10, 2021).
- [90] R. Claridad, Tensile test for reinforced glass fiber rebar, (n.d.).  
<https://www.youtube.com/watch?v=zDMX-0mAESQ> (accessed December 10, 2021).

## List of Publications

### [Journal papers]

1. Nam Van Vo and Isamu Yoshitake, Assessing shear-lag effect on pultruded FRP rods based on a numerical simulation, *International Journal of GEOMATE*, 21 (2021) 167–176. doi: <https://doi.org/10.21660/2021.84.j2163>.
2. Van-Nam Vo, Sy-Ngoc Nguyen, Isamu Yoshitake, Predicting failure modes and load-capacity of fiber-reinforced polymer rods in adhesively bonded anchorages based on numerical modeling, *Construction and Building Materials*, 318 (2022) 1–12. doi: <https://doi.org/10.1016/j.conbuildmat.2021.126135>.

### [Conference paper]

3. Nam Van Vo and Isamu Yoshitake, A numerical simulation of shear-lag behavior in fiber reinforced polymer (FRP) rod, in: Proceedings of the 6th International Conference of Construction Materials, 2020.